J. Non-Newtonian Fluid Mech. 166 (2011) 593–606

Contents lists available at ScienceDirect

Journal of Non-Newtonian Fluid Mechanics

journal homepage: www.elsevier.com/locate/jnnfm

A mean-field anisotropic diffusion model for unentangled polymeric liquids and semi-dilute solutions: Model development and comparison with experimental and simulation data

J.M. Kim [a], P.S. Stephanou [b], B.J. Edwards [a,*], B. Khomami [a]

[a] Department of Chemical and Biomolecular Engineering, University of Tennessee, Knoxville, TN 37996, United States
[b] Department of Chemical Engineering, University of Patras, GR26504, Greece

ARTICLE INFO

Article history:
Received 21 September 2010
Received in revised form
14 December 2010
Accepted 28 December 2010
Available online 11 January 2011

Keywords:
Anisotropic diffusion
Brownian dynamics
Bead-spring chain model
Coarse-graining and mesoscopic modeling

ABSTRACT

A coarse-grained mesoscopic model was developed based on the *ansatz* that a specific polymer molecule diffuses through the nearby neighboring chains more easily in the direction parallel to its molecular axis than perpendicular to it. This idea is modeled using a mean-field approach in terms of an anisotropic diffusion matrix, which represents enhanced diffusion along the chain background once a significant degree of molecular extension and orientation has developed in response to an applied flow field. The rheological and microstructural characteristics of this model are examined and compared with atomistic nonequilibrium molecular dynamics (NEMD) simulation data of short-chain polyethylene liquids and experiments of semi-dilute DNA solutions under shear flow. Rheological and microstructural properties examined include the viscosity, normal stress coefficients, conformation tensor, *etc.*, to gauge the usefulness of the model. In addition, this model was further coarse-grained to the continuum level through pre-averaging, and was also compared with the simulation and experimental data to examine the relationships between different levels of description on the rheological and structural properties of unentangled polymeric materials under shear flow.

At the mesoscopic level, the polymer molecules are modeled as bead-spring chains using the finitely extensible nonlinear elastic (FENE) force law. Brownian dynamics (BD) simulations of this coarse-grained model displayed remarkable quantitative agreement with NEMD simulations of dense liquids and experiments of semi-dilute DNA solutions for system properties with a single adjustable parameter representing the relative magnitude of diffusive enhancement along the chain backbone. Furthermore, the BD simulations revealed the dependence of system response on the chain stretching at low values of Weissenberg number (*Wi*) and on the rotational motion of individual chains induced by shear flow at high values of *Wi*, similarly to the NEMD simulation data. The continuum model matched the mesoscopic model at low shear rates, but greatly diverged at high values of *Wi* where the tumbling dynamics of the individual chains dominated the system response. This provides direct evidence that the onset of rotational motion under shear in these liquids is responsible for the well-known breakdown in pre-averaged constitutive equations at the continuum level of description. Furthermore, a possible explanation of the shear stress plateau at intermediate ranges of shear rate is offered for experimental data of semi-dilute solutions, wherein this phenomenon occurs with the onset of chain rotation within these fluids.

1. Introduction

The description of fast flows of macromolecular fluids has proven to be a difficult challenge for rheologists. Many theories were proposed during the 20th century for the purpose of explaining the rheological and morphological responses of the liquids under flow, but they invariably diverged from experiment at high Weissenberg number, *Wi*, regardless of their degree of success at describing the linear and weakly nonlinear viscoelastic regimes. Many reasons have been proposed for these discrepancies at high *Wi*, such as the onset of "convected constraint release," the failure of closure approximations, destruction of polymer network junctures, *etc.* [1]. The second of these reasons, closure approximations, has been a particularly egregious offender, and many instances have been documented of their failure to describe even qualitatively the theories that they were used to close [*e.g.*, 2–7].

The first decade of the twenty-first century has elucidated another possibility as an explanation for the failure of rheological

* Corresponding author. Tel.: +1 865 974 9596.
E-mail address: bje@utk.edu (B.J. Edwards).

0377-0257/$ – see front matter © 2011 Elsevier B.V. All rights reserved.
doi:10.1016/j.jnnfm.2010.12.011

theories under high *Wi* steady shear flow, at least for low molecular weight short-chain liquids and semi-dilute solutions of linear, long-chain macromolecules. These materials are composed primarily of unentangled chains that are free to move segmentally as individual entities, although bulk chain movement is still constrained by the surrounding molecules. Evidence of this explanation has been provided by both simulation and experiment, each of which indicates that a significant degree of individual chain rotation and tumbling occurs under high *Wi* shear flow. Indeed, this molecular rotation corresponds to *Wi* regimes wherein intriguing phenomena are evidenced in the measured rheological response of simple experiments, such as the stress plateau observed in shear experiments of semi-dilute and concentrated polymeric solutions, as discussed later.

The possibility of rotational molecular tumbling as a root cause of interesting rheological features as observed in experiment should come as no surprise to liquid crystal theorists. For many years, it was observed that the steady-shear, first normal-stress difference of a liquid-crystalline fluid would exhibit two sign changes with increasing shear rate, one moving from positive to negative at a lower shear rate, and one changing back from negative to positive at a higher shear rate. Indeed, this subject area provides one of the classic examples of the failure of closure and pre-averaging approximations. Thirty years ago, Doi [8] derived a theory of liquid crystalline dynamics expressed in terms of a diffusion equation for the probability distribution function of the orientation of a rod-like molecule. With limited computational power available at that time, he immediately reduced this theory to a continuum-level description written in terms of a second-rank order parameter tensor, but was forced to introduce a closure approximation in order to do so [8]. The predicted behavior of the pre-averaged model indicated a purely flow-aligning behavior of the rod-like molecules, and a monotonically increasing first normal-stress difference for all values of shear rate. Years later, researchers discovered that the suppression of molecular rotation at low and intermediate shear rates was the probable cause of this departure from experiment [4]. Subsequent simulation, either in terms of the original expression for the probability distribution function [9] or in terms of the second-rank tensor evolution equation developed without a closure approximation or pre-averaging [10–13], demonstrated unequivocally that the suppression of molecular rotation was responsible for the failure of the closed model to describe the peculiar rheological features of the first normal-stress difference under shear flow. Despite this knowledge gained 20 years ago, the idea of pre-averaging or closure approximations inducing a loss of systematic rotational motion of the constituent polymer chains has only recently been considered as a possible mechanism for explaining the unusual features of high *Wi* shear flow.

Recent advances in rheo-optical imaging have made possible direct observation of the dynamics of individual molecules comprising dilute and semi-dilute solutions under shear flow using fluorescently labeled DNA macromolecules dissolved in water [14–18]. These experiments have revealed the rich dynamical behavior of macromolecular solutions and the individuality of expression of single chains within them. Such specific dynamical events as chain stretching, recoiling, and tumbling were observed as functions of shear rate.

Recent simulations have also captured this individuality of the dynamical expression of single chains in dense short-chain liquids under shear [19,20]. In particular, nonequilibrium molecular dynamics (NEMD) simulations of the linear polyethylene liquid $C_{78}H_{158}$ have revealed distinct, shear-rate dependent timescales associated with the rotation of the molecules at high *Wi*, thus assigning specific periods to tumbling cycles of individual chains. Kim et al. [19,20] conjectured that the onset of fast molecular rotation, which occurred at a *Wi* in the range of 2–5, was responsible for many of the failures of pre-averaged rheological theories to describe the properties of highly shearing liquids. Furthermore, Baig et al. [21] noted the existence of an apparent critical value of shear stress for the analogous liquid, $C_{50}H_{102}$, at which the stress-optical law begin to diverge from simulated data. This critical shear stress occurred within the same range of *Wi* as noted above, which raises the possibility of an association between molecular tumbling and the breakdown of the stress-optical law at high *Wi*.

The purpose of this article is to demonstrate that the rotation and tumbling of individual macromolecules is responsible for much of the peculiar behavior of unentangled chain liquids and solutions at high *Wi*. To achieve this goal, it is first necessary to derive a mesoscopic-level model that is able to quantify the molecular rotation evident in experiment and atomistic simulation, and then to examine the rheological consequences that it implies. Furthermore, it is necessary to examine the effect on this model of the suppression of individual chain rotation, which can be accomplished by reducing this mesoscopic model to a continuum model in terms of a second-rank conformation tensor by introducing pre-averaging and closure approximations.

In this article, a mean-field mesoscopic model is developed to mimic the anisotropic diffusive motion of an arbitrary chain within the confines of tube-like structures that are formed by the surrounding stretched chains at high *Wi*. These tube-like structures have been noticed in recent simulations of short-chain, unentangled polyethylenes [22,23], and their apparent dimensions were calculated by Kim et al. [23] for both shear and planar elongational flows. The NEMD simulations have shown that a given molecule will diffuse through a tube-like structure, formed by the surrounding stretched chains, during its periodic tumbling cycle [19,20]; however, this diffusive motion is highly anisotropic since the chain can move more freely along its own (and the tube's) axis rather than perpendicular to it.

The model was derived using a bead-spring chain with a finitely extensible nonlinear elastic (FENE) force law for each spring and an anisotropic diffusion tensor. Brownian dynamics (BD) simulations were used to examine the model's behavior under shear flow, and a pre-averaged version was obtained at the level of second-rank conformation tensors representing the configurations of the individual chain segments. An even more coarse-grained dumbbell model was derived and examined as well.

2. Model development

The bead-spring chain model consists of N identical spherical beads connected by $N-1$ FENE springs. The FENE spring force law for each spring $\left(\mathbf{F}_i^S\right)$ is written as

$$F_{\alpha,i}^S = Kh_iQ_\alpha^i, \quad h_i = \frac{1}{1-\left|Q^i\right|^2/b_s}, \quad i = 1,2,\ldots,N-1, \tag{1}$$

where the K and $\mathbf{Q}^i$ denote the elastic spring constant and the connector vector of the ith spring, respectively. The b_s represents the maximum extensibility of all springs. The h_i determines the specific form of elasticity inherent to the spring; when $h_i = 1$, for example, the force law devolves into the linear Hookean spring. Note that Greek indices refer to the components of a Cartesian coordinate system and that the Einstein summation convention is assumed.

For the unentangled liquids and semi-dilute solutions under consideration, a mean-field assumption is assumed to describe the effects of the oriented surrounding molecules on a test chain with the properties set forth above. This mean field is expressed through an anisotropic diffusion tensor,

$$\zeta_{\alpha\beta,i}^{-1} = \zeta_0^{-1}\left[\alpha\delta_{\alpha\beta} + (1-\alpha)\tilde{Q}_\alpha^i\tilde{Q}_\beta^i\right], \tag{2}$$

where $\delta_{\alpha\beta}$ denotes the unit tensor, $\tilde{Q}^i_\alpha \equiv \sqrt{K/k_BT}Q^i_\alpha$ refers to the dimensionless connector vector, and ζ_0^{-1} is the reciprocal of a frictional drag coefficient, assumed to be the same for each of the identical beads. The dimensionless parameter α quantifies the influences on an individual chain from its surrounding chains, which are represented within the mean-field *ansatz* via the degree of anisotropy in the diffusion matrix. Note that this form of the diffusion tensor recovers the isotropic case when $\alpha = 1$.

It is very important to understand the nature of this anisotropic diffusion tensor, and how it compares to previous attempts to introduce anisotropicity into kinetic theory models of polymeric liquids. In the present case, it is specifically intended to model the test chain diffusion in terms of a diffusivity coefficient parallel, $\Lambda_{||}$, and perpendicular, $\Lambda_\perp$, to the direction of the connector vector of each spring.

In prior NEMD simulations of shear flow [22,23], the test liquid $C_{78}H_{158}$ was conjectured to form tube-like structures composed of highly extended molecules, through which other molecules rotated in hairpin configurations, as had also been observed in experiments of dilute DNA solutions [17,18]. Recent evidence of Kim et al. [19,20] has confirmed this hypothesis, revealing definite correlations and timescales associated with tumbling events of individual molecules passing through tube-like structures of highly extended molecules. In light of this new evidence, it is possible that a realistic model of these linear, short-chain, unentangled molecular systems could be modeled in terms of a test chain placed in a mean-field that quantified the surrounding tube-like structure of highly extended chains through an anisotropic diffusion tensor, in which the diffusivity coefficient parallel to the chain or segmental backbone was greater than the coefficient perpendicular to the chain backbone.

The anisotropic form of the diffusion tensor possessing the fundamental properties described in the prior paragraph, as expressed by Eq. (2), has been derived before [24–27] as

$$\Lambda^i_{\alpha\beta} \equiv \Lambda_\perp \delta_{\alpha\beta} + (\Lambda_{||} - \Lambda_\perp)\tilde{Q}^i_\alpha \tilde{Q}^i_\beta. \tag{3}$$

This expression may be rewritten as

$$\Lambda^i_{\alpha\beta} \equiv \Lambda_{||}\left[\alpha\delta_{\alpha\beta} + (1-\alpha)\tilde{Q}^i_\alpha \tilde{Q}^i_\beta\right], \tag{4}$$

where the dimensionless parameter α appearing in Eqs. (2) and (4) is defined as the ratio of the parallel and perpendicular diffusion coefficients, $\alpha \equiv \Lambda_\perp/\Lambda_{||}$. This expression precisely quantifies the anisotropic diffusion tensor with respect to motions parallel and perpendicular to the molecular contour for linear molecules, such that translational diffusion is easier in the direction parallel to the chain backbone when $\alpha < 1$. When $\alpha = 1$, there is no preferential direction of translational motion, and Eqs. (2) and (4) must reduce to the isotropic diffusion tensor (or reciprocal of the drag coefficient). This implies that $\Lambda_{||} = \zeta_0^{-1}$ [25,28,29], which motivates the choice of symbols in Eq. (2).

During the previous three decades, various coarse-grained mesoscopic models have been proposed that introduce some form of anisotropic drag or mobility into the kinetic theory of elastic dumbbells. Giesekus [30,31] introduced an anisotropic mobility tensor that bears a similar form to Eq. (2),

$$\zeta^{-1}_{\alpha\beta,i} = \zeta_0^{-1}\left[(1-\alpha)\delta_{\alpha\beta} + \alpha\tilde{Q}^i_\alpha\tilde{Q}^i_\beta\right]; \tag{5}$$

however, this form of mobility is conceptually different from a modeling perspective than the anisotropic diffusion tensor with the form of Eq. (3) in the sense that the latter is a direct product of transport modeling in terms of physically meaningful diffusion coefficients, which are required to remain positive at all times. Bird and Deaguiar [32] developed an "encapsulated dumbbell" model based on a modified form of Stokes' law [27], which is exactly the same as Eq. (2), and an anisotropic Brownian force, corresponding to an additional tensorial quantity,

$$\xi^{-1}_{\alpha\beta} = \beta\delta_{\alpha\beta} + (\chi - \beta)\frac{Q_\alpha Q_\beta}{\left|Q^2\right|}, \tag{6}$$

with χ and β defined as parameters that quantified the degree of anisotropicity. Phan-thien and Atkinson [33] demonstrated that the encapsulated dumbbell model violated the fluctuation-dissipation theorem; however, in the absence of the anisotropic Brownian force, there was no violation of this principle. Using the generalized bracket methodology, Beris and Edwards [25,29] derived a modified form of the encapsulated dumbbell model that satisfied this theorem. Öttinger [34] also proposed a "consistently averaged" form of the Oseen-Burgers tensor, which shared the form of Eq. (6) under the assignments $\beta = 1$ and $\chi = 2$.

2.1. Atomistic level of description

The Siepmann–Karaboni–Smit (SKS) united-atom model for linear alkanes [35] was applied to NEMD simulation due to its wide employment for simulating equilibrium thermodynamics properties and rheological behavior of alkanes and polyethylenes. However, the rigid bond in the original united-atom model between adjacent atoms was replaced with a harmonic potential function to relieve issues related to stiff integrations at small timescales. In this model, the LJ potential for the intermolecular and intramolecular atomic interactions is written as,

$$V_{LJ}(r) = 4\varepsilon_{ij}\left[\left(\frac{\sigma_{ij}}{r}\right)^{12} - \left(\frac{\sigma_{ij}}{r}\right)^{6}\right]. \tag{7}$$

The parameters ε_{ij} and σ_{ij} were approximated through Berthelot mixing rules. The ε_{CH_2} and ε_{CH_3} were 47 K and 114 K, respectively, and the σ_{CH_2} and σ_{CH_3} were 3.93 Å each. Only atoms that were separated by more than three bonds were considered for the intramolecular LJ interaction energy. A cut-off distance, r_c, of $2.5\sigma_{CH_2}$ (9.825 Å) was chosen for the LJ potential and the potential energy was assumed to vanish beyond the cut-off distance. The bond-stretching interaction is defined by a harmonic potential function,

$$V_{str}(l) = \frac{1}{2}k_{str}(l - l_{eq})^2, \tag{8}$$

where the bond-stretching constant was $k_{str}/k_B = 452,900$ K/Å^2 and the equilibrium length was $l_{eq} = 1.54$ Å. The bond-bending interaction was governed by a harmonic potential,

$$V_{ben}(\theta) = \frac{1}{2}k_{ben}(\theta - \theta_{eq})^2. \tag{9}$$

The equilibrium angle and the bond-bending constant in this expression were $\theta_{eq} = 114^\circ$, and $k_{ben}/k_B = 62,500$ K/rad^2, respectively. The bond-torsional interaction developed by Jorgensen et al. [36] was written as

$$V_{tor}(\phi) = \sum_{m=0}^{3} a_m(\cos\phi)^m. \tag{10}$$

The parameters a_0/k_B, a_1/k_B, a_2/k_B, and a_3/k_B in this equation were set at 1010 K, 2019 K, 136.4 K, and 3165 K, respectively.

2.2. Mesoscopic level of description

According to kinetic theory of polymeric liquids [27], three external forces act on each bead of a bead-spring model; the hydrodynamic drag force, $\mathbf{F}^H_i$, the effective spring force, $\mathbf{F}^E_i$, and the

Brownian force, $\mathbf{F}_i^B$. Therefore, a force balance on the beads may be expressed as

$$\mathbf{F}_{\alpha,i}^H + \mathbf{F}_{\alpha,i}^E + \mathbf{F}_{\alpha,i}^B = 0, \quad i = 1, 2, \ldots, N, \tag{11}$$

where N is the total number of beads. Notice, as is usually the case, that we have neglected inertial contributions [37]. In Eq. (11), the hydrodynamic drag force on each bead $\left(\mathbf{F}_i^H\right)$ is quantified by Stokes's law, which is expressed as

$$\mathbf{F}_{\alpha,i}^H = -\zeta_{\alpha\beta}^i \left(\dot{r}_\beta^i - v_\beta^i\right). \tag{12}$$

The $\dot{r}_\beta^i$ and $v_\beta^i \left(= v_\beta^0 + \kappa_{\beta\alpha} r_\alpha^i\right)$ denote components of the velocity and streaming velocity profile of the ith bead, respectively, where $\kappa_{\beta\alpha}$ is a component of the transpose of the velocity gradient tensor and r_α^i is the position vector of ith bead. The $\zeta_{\alpha\beta}^i$ represents an anisotropic friction matrix, which is the inverse of an anisotropic diffusion matrix. The effective spring force on bead i $\left(\mathbf{F}_i^E\right)$ is expressed as

$$\mathbf{F}_{\alpha,i}^E = -\frac{\partial \phi}{\partial r_\alpha^i}, \tag{13}$$

where ϕ denotes the spring potential energy. The Brownian force on each bead $\left(\mathbf{F}_i^B\right)$ is taken as

$$\mathbf{F}_{\alpha,i}^B = -k_B T \frac{\partial}{\partial r_\alpha^i} \ln \Psi, \tag{14}$$

where k_B and T denote the Boltzmann constant and temperature, respectively. The $\Psi\left(\left\{\mathbf{r}^i\right\}, t\right)$ represents the configurational distribution function. By substituting Eqs. (12)–(14) into (11), and rearranging the equation, one obtains the equations of motion for the position vectors, which are

$$\dot{r}_\alpha^i = v_\alpha^0 + \kappa_{\alpha\beta} r_\beta^i - \zeta_{\alpha\beta,i}^{-1} \left[F_{\beta,i}^E + \frac{k_B T}{\Psi} \frac{\partial \Psi}{\partial r_\beta^i}\right]. \tag{15}$$

From kinetic theory, the continuity equation of the distribution function $\Psi\left(\left\{\mathbf{r}^i\right\}, t\right)$ is expressed as

$$\frac{\partial \Psi}{\partial t} = -\sum_{i=1}^{N} \frac{\partial}{\partial r_\alpha^i} \left(\dot{r}_\alpha^i \Psi\right). \tag{16}$$

Therefore, the diffusion equation for $\Psi\left(\left\{r^i\right\}, t\right)$ can be obtained by inserting Eq. (15) into Eq. (16), which results in the expression

$$\frac{\partial \Psi}{\partial t} = -\sum_{i=1}^{N} \frac{\partial}{\partial r_\alpha^i} \left\{\left(v_\alpha^0 + \kappa_{\alpha\beta} r_\beta^i \psi - \zeta_{\alpha\beta,i}^{-1} F_{\beta,i}^E\right) \Psi - k_B T \zeta_{\alpha\beta,i}^{-1} \frac{\partial \Psi}{\partial r_\beta^i}\right\}. \tag{17}$$

For present purposes, this deterministic diffusion equation for the probability distribution function is rewritten in terms of a stochastic differential equation (SDE), which can then be split into a coupled set of evolution equations for the position vectors. The specific form of the diffusion equation for the distribution function is converted into the corresponding form of a SDE according to [38]

$$\frac{\partial \Psi}{\partial t} = -\sum_{i=1}^{N} \left\{\frac{\partial}{\partial r_\alpha^i}\left[C_\alpha^i \Psi\right] + \frac{1}{2} \frac{\partial}{\partial r_\alpha^i} \frac{\partial}{\partial r_\beta^i}\left[\zeta_{\alpha\beta,i}^{-1} \Psi\right]\right\} \rightarrow dr_\alpha^i = C_\alpha^i dt + B_{\gamma\alpha}^i dW_\gamma^i, \tag{18}$$

where $\mathbf{W}$ represents the Wiener process. $\mathbf{B}^i$ is the 'square root' of $\zeta_{\alpha\beta,i}^{-1} (= B_{\alpha\gamma}^i B_{\gamma\beta}^i)$, and is chosen as a lower triangular 3×3 matrix using Cholesky decomposition [38], which satisfies

$$\mathbf{B}^i \cdot \left(\mathbf{B}^i\right)^T = \begin{bmatrix} B_{11}^i & 0 & 0 \\ B_{21}^i & B_{22}^i & 0 \\ B_{31}^i & B_{32}^i & B_{33}^k \end{bmatrix} \cdot \begin{bmatrix} B_{11}^i & B_{12}^i & B_{13}^i \\ 0 & B_{22}^i & B_{23}^i \\ 0 & 0 & B_{33}^i \end{bmatrix} = \zeta_{\alpha\beta,i}^{-1}. \tag{19}$$

Hence, Eq. (17) should be rearranged to have the specific form of configurational distribution as in Eq. (18) at the mesoscopic level,

$$\frac{\partial \Psi}{\partial t} = -\sum_{i=1}^{N} \left[\frac{\partial}{\partial r_\alpha^i} \left\{\left(v_\alpha^0 + \kappa_{\alpha\beta} r_\beta^i - \zeta_{\alpha\beta,i}^{-1} F_{\beta,i}^E + k_B T \frac{\partial \zeta_{\alpha\beta,i}^{-1}}{\partial r_\beta^i}\right) \Psi\right\}\right] + k_B T \sum_{i=1}^{N} \frac{\partial}{\partial r_\alpha^i} \frac{\partial}{\partial r_\beta^i} \left(\zeta_{\alpha\beta,i}^{-1} \Psi\right). \tag{20}$$

Then one can obtain a SDE for the position vectors using Eqs. (18) and (19),

$$dr_\alpha^i = \left(v_\alpha^0 + \kappa_{\alpha\beta} r_\beta^i - \zeta_{\alpha\beta,i}^{-1} F_{\beta,i}^E + k_B T \frac{\partial \zeta_{\alpha\beta,i}^{-1}}{\partial r_\beta^i}\right) dt + B_{\alpha\beta}^i dW_\beta^i. \tag{21}$$

The effective spring force on bead i $\left(\mathbf{F}_i^E\right)$ combined with the anisotropic diffusion tensor is written as

$$\zeta_{\alpha\beta,i}^{-1} F_{\beta,i}^E = \begin{cases} \zeta_{\alpha\beta,1}^{-1} F_{\beta,1}^S & \text{if } i = 1 \\ \zeta_{\alpha\beta,i}^{-1} F_{\beta,i}^S - \zeta_{\alpha\beta,i-1}^{-1} F_{\beta,i-1}^S & \text{if } 1 < i < N, \\ -\zeta_{\alpha\beta,N-1}^{-1} F_{\beta,N-1}^S & \text{if } i = N \end{cases} \tag{22}$$

where $\mathbf{F}_i^S$ is the spring force associated with spring i.

Since the anisotropic diffusion matrix and stress tensor depend on the connector vector between adjacent beads, it is convenient to express the equation of motion using this vector. Substitution of the definition of the connector vector $\left(Q_\alpha^i = r_\alpha^{i+1} - r_\alpha^i\right)$ into Eqs. (21) and (22) results in the SDE for the evolution of a connector vector,

$$dQ_\alpha^i = \left(\kappa_{\alpha\beta} Q_\beta^i - \sum_{k=1}^{N-1} A_{ik} \left[\zeta_{\alpha\beta,k}^{-1} F_{\beta,k}^S + k_B T \frac{\partial \zeta_{\alpha\beta,k}^{-1}}{\partial Q_\beta^k}\right]\right) dt + B_{\alpha\beta}^i \left(dW_\beta^{i+1} - dW_\beta^i\right), \tag{23}$$

where

$$A_{ik} = \begin{cases} 2 & \text{if } \left|i-k\right| = 0 \\ -1 & \text{if } \left|i-k\right| = 1 \\ 0 & \text{otherwise} \end{cases}.$$

The A_{ik} are the elements of the Rouse matrix [39]. Eq. (23) can be made dimensionless with the transformations

$$\begin{aligned} &Q_\alpha = \sqrt{\frac{k_B T}{K}} \tilde{Q}_\alpha, \quad t = \frac{L}{V_c} \tilde{t}, \quad \tau_R = \frac{\zeta_0}{4K} = \tilde{\tau}_R \frac{L}{V_c}, \\ &Wi = \dot{\gamma} \tau_R = \frac{V_c}{L} \tau_R, \quad dW_\alpha^i = \sqrt{dt} d\tilde{W}_\alpha^i \\ &\zeta_{\alpha\beta,k}^{-1} = \zeta_0^{-1} \tilde{\zeta}_{\alpha\beta,k}^{-1}, \quad \kappa_{\alpha\beta} = \frac{V_c}{L} \tilde{\kappa}_{\alpha\beta}, \quad F_\beta^S = \sqrt{K k_B T} \tilde{F}_\beta^S, \\ &B_{\alpha\beta}^i = \sqrt{2 k_B T \zeta_0^{-1}} \tilde{B}_{\alpha\beta}^i. \end{aligned} \tag{24}$$

Note that the terms with a tilde are dimensionless. The Wi is the Weissenberg number and τ_R is the Rouse time. The V_c and L are

arbitrary velocity and length scales, respectively. As a result, the dimensionless equation for dQ_α^i is

$$d\tilde{Q}_\alpha^i = \left(\tilde{\kappa}_{\alpha\beta}\tilde{Q}_\beta^i - \frac{1}{4Wi}\sum_{k=1}^{N-1} A_{ik}\left[\tilde{\zeta}_{\alpha\beta,k}^{-1}\tilde{F}_{\beta,k}^S + \frac{\partial \tilde{\zeta}_{\alpha\beta,k}^{-1}}{\partial \tilde{Q}_\beta^k} \right] \right) d\tilde{t} + \frac{1}{\sqrt{2Wi}}\tilde{B}_{\alpha\beta}^i \left(d\tilde{W}_\beta^{i+1} - d\tilde{W}_\beta^i \right). \quad (25)$$

Finally, we obtain the stochastic evolution equation of the connector vector by substituting the FENE spring force law and the anisotropic diffusion matrix into Eq. (25),

$$d\tilde{Q}_\alpha^i = \left(\tilde{\kappa}_{\alpha\beta}\tilde{Q}_\beta^i - \frac{1}{4Wi}\sum_{k=1}^{N-1} A_{ik}\left\{ h_k\left[\alpha + (1-\alpha)\left| \left(\tilde{Q}_\beta^k\right)^2 \right| \right]\tilde{Q}_\alpha^k + 2(1-\alpha)\tilde{Q}_\alpha^k \right\} \right) d\tilde{t} + \frac{1}{\sqrt{2Wi}}\tilde{B}_{\alpha\beta}^i \left(d\tilde{W}_\beta^{i+1} - d\tilde{W}_\beta^i \right). \quad (26)$$

2.3. Continuum level of description

At the continuum level of description, the exact locations of the beads become irrelevant as only macroscopic averages are quantified and described. To indicate that the distribution function is independent of the location of the position of the beads, a factorization was performed, $\Psi\left(\left\{\mathbf{r}^N\right\}, t\right) = n\psi\left(\left\{\mathbf{Q}^{N-1}\right\}, t\right)$, where n is the number density of chains following Bird et al. [27]. With this factorization, Eq. (16) was written as

$$\frac{\partial \psi}{\partial t} = -\sum_{i=1}^{N}\frac{\partial}{\partial r_\gamma^i}\left(\psi \dot{r}_\gamma^i\right),$$

or, via direct substitution,

$$\frac{\partial \psi}{\partial t} = -\sum_{i=1}^{N-1}\frac{\partial}{\partial Q_\alpha^i}\left\{ \kappa_{\alpha\beta}Q_\beta^i\psi - \sum_{k=1}^{N-1}A_{ik}\zeta_{\alpha\beta,k}^{-1}\left[F_{\beta,k}^S\psi + k_BT\frac{\partial \psi}{\partial Q_\beta^k} \right] \right\}. \quad (27)$$

The diffusion equation of the distribution function was further coarse-grained through pre-averaging. By multiplying $Q_\alpha^i Q_\beta^i$ on each side of Eq. (27) and then integrating over all the configuration space, one can derive the evolution equation for $\left\langle Q_\alpha^i Q_\beta^i \right\rangle$, which is

$$\frac{\partial}{\partial t}\left\langle Q_\alpha^i Q_\beta^i \right\rangle = \kappa_{\alpha\varepsilon}\left\langle Q_\beta^i Q_\varepsilon^i \right\rangle + \kappa_{\beta\varepsilon}\left\langle Q_\alpha^i Q_\varepsilon^i \right\rangle + \sum_{k=1}^{N-1}A_{ik}\left[2k_BT\left\langle \frac{\partial}{\partial Q_\varepsilon^k}\zeta_{\alpha\varepsilon,k}^{-1}Q_\beta^k \right\rangle + 2k_BT\left\langle \frac{\partial}{\partial Q_\varepsilon^k}\zeta_{\beta\varepsilon,k}^{-1}Q_\alpha^k \right\rangle - 2\left\langle \zeta_{\alpha\varepsilon,k}^{-1}Q_\beta^k F_{\alpha,k}^S \right\rangle - 2\left\langle \zeta_{\beta\varepsilon,k}^{-1}Q_\alpha^k F_{\beta,k}^S \right\rangle \right], \quad (28)$$

for $i = 1, 2, \ldots, N-1$. Here, the definition of the average property, $\langle E \rangle = \int E\psi\, d\mathbf{Q}^i$, is used. The upper convected time derivative is defined by

$$\frac{D}{Dt}\left\langle Q_\alpha^i Q_\beta^i \right\rangle = \frac{\partial}{\partial t}\left\langle Q_\alpha^i Q_\beta^i \right\rangle - \kappa_{\alpha\varepsilon}\left\langle Q_\beta^i Q_\varepsilon^i \right\rangle - \kappa_{\beta\varepsilon}\left\langle Q_\alpha^i Q_\varepsilon^i \right\rangle. \quad (29)$$

Thus, Eq. (28) can be also written as

$$\frac{D}{Dt}\left\langle Q_\alpha^i Q_\beta^i \right\rangle = \sum_{k=1}^{N-1}A_{ik}\left[2k_BT\left\langle \frac{\partial}{\partial Q_\varepsilon^k}\zeta_{\alpha\varepsilon,k}^{-1}Q_\beta^k \right\rangle + 2k_BT\left\langle \frac{\partial}{\partial Q_\varepsilon^k}\zeta_{\beta\varepsilon,k}^{-1}Q_\alpha^k \right\rangle - 2\left\langle \zeta_{\alpha\varepsilon,k}^{-1}Q_\beta^k F_{\alpha,k}^S \right\rangle - 2\left\langle \zeta_{\beta\varepsilon,k}^{-1}Q_\alpha^k F_{\beta,k}^S \right\rangle \right]. \quad (30)$$

Eq. (30) can be also expressed in dimensionless form using the transformations of Eq. (24),

$$\frac{D}{D\tilde{t}}\left\langle \tilde{Q}_\alpha^i \tilde{Q}_\beta^i \right\rangle = \sum_{k=1}^{N-1}A_{ik}\left[\frac{1}{2}\left\langle \frac{\partial}{\partial \tilde{Q}_\varepsilon^k}\tilde{\zeta}_{\alpha\varepsilon,k}^{-1}\tilde{Q}_\beta^k \right\rangle + \frac{1}{2}\left\langle \frac{\partial}{\partial \tilde{Q}_\varepsilon^k}\tilde{\zeta}_{\beta\varepsilon,k}^{-1}\tilde{Q}_\alpha^k \right\rangle - \frac{1}{2}\left\langle \tilde{\zeta}_{\alpha\varepsilon,k}^{-1}\tilde{Q}_\beta^k\tilde{F}_{\alpha,k}^S \right\rangle - \frac{1}{2}\left\langle \tilde{\zeta}_{\beta\varepsilon,k}^{-1}\tilde{Q}_\alpha^k\tilde{F}_{\beta,k}^S \right\rangle \right]. \quad (31)$$

Introducing the FENE spring force law and the anisotropic diffusion matrix into Eq. (31) gives

$$\frac{D}{D\tilde{t}}\left\langle \tilde{Q}_\alpha^i \tilde{Q}_\beta^i \right\rangle = \sum_{k=1}^{N-1}A_{ik}\left[-h_k(1-\alpha)\left\langle \tilde{Q}_\varepsilon^k\tilde{Q}_\varepsilon^k\tilde{Q}_\alpha^k\tilde{Q}_\beta^k \right\rangle - h_k\alpha\left\langle \tilde{Q}_\alpha^k\tilde{Q}_\beta^k \right\rangle + 5(1-\alpha)\left\langle \tilde{Q}_\alpha^k\tilde{Q}_\beta^k \right\rangle + \alpha\delta_{\alpha\beta} \right]. \quad (32)$$

In Eq. (32), the fourth-rank tensor can be written in terms of second-rank tensors using any one of the multitude of closure approximations that have been proposed in the literature, such as the one proposed by Doi [8], which has been shown to satisfy time-structure invariance by Edwards and Öttinger [2]: $\left\langle Q_\alpha^k Q_\gamma^k Q_\varepsilon^k Q_\beta^k \right\rangle \delta_{\gamma\varepsilon} \approx \left\langle Q_\alpha^k Q_\gamma^k \right\rangle \left\langle Q_\varepsilon^k Q_\beta^k \right\rangle \delta_{\gamma\varepsilon}$. In this work, the closure

$$\left\langle \tilde{Q}_\varepsilon^k\tilde{Q}_\varepsilon^k\tilde{Q}_\alpha^k\tilde{Q}_\beta^k \right\rangle \Rightarrow \frac{5}{3}\left\langle \tilde{Q}_\varepsilon^k\tilde{Q}_\varepsilon^k \right\rangle \left\langle \tilde{Q}_\alpha^k\tilde{Q}_\beta^k \right\rangle \quad (33)$$

was used because it most closely matches the assumed closure used to develop the FENE-P model; however, the former closure approximation yields a result that more closely resembles the Giesekus model. Under the assumption of Eq. (33), the constitutive equation at the continuum level is obtained as

$$\frac{D}{D\tilde{t}}\left\langle \tilde{Q}_\alpha^i \tilde{Q}_\beta^i \right\rangle = \sum_{k=1}^{N-1}A_{ik}\left\{ -h_k\left[\frac{5}{3}(1-\alpha)\left\langle \tilde{Q}_\varepsilon^k\tilde{Q}_\varepsilon^k \right\rangle + \alpha \right]\left\langle \tilde{Q}_\alpha^k\tilde{Q}_\beta^k \right\rangle + 5(1-\alpha)\left\langle \tilde{Q}_\alpha^k\tilde{Q}_\beta^k \right\rangle + \alpha\delta_{\alpha\beta} \right\}, \quad (34)$$

for $i = 1, 2, \ldots, N-1$.

Another coarse-graining procedure was performed to reduce the mesoscopic model to the dumbbell level of description using only a single FENE spring and expressed in terms of the conformation tensor. The dimensionless conformation tensor is written as

$$\tilde{C}_{\alpha\beta} = \left\langle \tilde{R}_\alpha\tilde{R}_\beta \right\rangle, \quad \tilde{R}_\alpha = \sum_{i=1}^{N-1}\tilde{Q}_\alpha^i = \tilde{r}_\alpha^N - \tilde{r}_\alpha^1, \quad (35)$$

where $\tilde{r}_\alpha^i$ denotes the dimensionless position vector of ith bead. This quantity can be used to derive a dumbbell model in terms of a single spring that is expressed in terms of this variable, which recovers the typical FENE dumbbell model for $\alpha = 1$ and $N = 2$:

$$\tilde{C}_{\alpha\beta} = \left\langle \tilde{R}_\alpha\tilde{R}_\beta \right\rangle = \left\langle \tilde{Q}_\alpha\tilde{Q}_\beta \right\rangle, \quad \frac{D}{D\tilde{t}}\tilde{C}_{\alpha\beta} = -h\left[\frac{5}{3}(1-\alpha)tr\tilde{C} + \alpha \right]\tilde{C}_{\alpha\beta} + 5(1-\alpha)\tilde{C}_{\alpha\beta} + \alpha\delta_{\alpha\beta}. \quad (36)$$

3. Simulation method

3.1. Atomistic level

The *NVT* NEMD simulations of the short-chain polyethylene liquid ($C_{78}H_{158}$) were performed at the atomistic level under shear flow to provide a fundamental description of the rheological characteristic functions, such as viscosity, and the dynamical

information concerning individual chains. Note that in all simulations under shear flow in this study, the flow direction is along the x axis and the flow gradient is along the y axis. The p-SLLOD equations of motion [40–42] combined with Nosé-Hoover thermostat [43,44] were applied as

$$\begin{aligned}\dot{\mathbf{q}}_{ia} &= \frac{\mathbf{p}_{ia}}{m_{ia}} + \mathbf{q}_{ia}\cdot\kappa^T,\\ \dot{\mathbf{p}}_{ia} &= \mathbf{F}_{ia} - \mathbf{p}_{ia}\cdot\kappa^T - \dot{\varsigma}\mathbf{p}_{ia},\\ \dot{\varsigma} &= \frac{p_\varsigma}{M},\quad \dot{p}_\varsigma = \sum_i\sum_a \frac{\mathbf{p}_{ia}^2}{m_{ia}} - DNk_BT,\quad M = DNk_BT\tau^2.\end{aligned} \tag{37}$$

Note that the p-SLLOD equations of motion are equivalent to the SLLOD equations of motion under shear flow [40–42]. The N, V, T represent total number of particles, simulation box volume, and absolute temperature, respectively. The $\mathbf{p}_{ia}$, $\mathbf{q}_{ia}$, and $\mathbf{F}_{ia}$ are the momentum, position, and force vector of the ath atom in the ith molecule. The m_{ia} is the mass of the ath atom in the ith molecule. The ς and P_ς stand for the position and momentum analogues of the Nosé-Hoover thermostat. The M refers to the inertial mass in Nosé-Hoover thermostat and the D refers system dimensionality (3). The τ denotes the characteristic time scale of the system. The κ^T denotes the transpose of the velocity gradient tensor and is defined as

$$\kappa^T = \begin{bmatrix} 0 & 0 & 0\\ \dot{\gamma} & 0 & 0\\ 0 & 0 & 0\end{bmatrix}. \tag{38}$$

These equations of motion were integrated using the reversible Reference System Propagator Algorithm (r-RESPA) with two timescales [45] under Lees–Edwards boundary condition, which guarantee periodic boundary conditions in the velocity-gradient direction for shear flow [46]. The NEMD simulation was performed at a temperature of 450 K. The simulation box size was carefully selected to prevent the introduction of system size effects. The length of simulation box in the flow direction (x) (=130.50 Å) was 30% longer than the fully stretched length of a short-chain polyethylene molecule (=99.45 Å) and the length of simulation box in velocity gradient (y) and neutral (z) (=54.00 Å) directions was also 10% longer than the radius of gyration of the average molecule at equilibrium. The density from experiment was adjusted to $\rho = 0.7640\,\mathrm{g/cm^3}$. Therefore, the numbers of chains and particles were calculated based on simulation box size and experimental density: 160 molecules and 12,480 particles. The KWW method was used to compute the Rouse relaxation time (or the longest rotational relaxation time), τ_R [47–50], which was determined to be 2300 ps for this linear $C_{78}H_{158}$ melt.

3.2. Mesoscopic level

At the mesoscopic level of description, the Brownian dynamics simulations for short-chain polyethylene liquids were carried out based on a bead-spring chain model with FENE springs and an anisotropic diffusion matrix. Eq. (26) was integrated using a new predictor–corrector algorithm, described in detail elsewhere [51]. The numbers of beads and springs per chain were fixed at reasonable values to obtain accurate results according to previous research [20]. A thousand identical chains with 15 springs and 16 beads each were used for the BD simulations. The fully stretched length of the bead-spring chain was matched to the atomistic molecules of the NEMD simulations. The maximum extensibility of each spring (b_s) was calculated using the expression

$$\begin{aligned} b_m &= \frac{3\times R_{max}^2}{\langle R^2\rangle_{eq}} = \frac{3\times 9890(\text{Å})^2}{1492(\text{Å})^2} \approx 20,\\ b_s &= \frac{b_m}{N^2} \approx 0.08889,\end{aligned} \tag{39}$$

where the R_{max} refers to the fully stretched, end-to-end length of a linear $C_{78}H_{158}$ molecule. The b_m and b_s denote the maximum extensibility of the entire molecule and each spring, respectively. The bead-spring model also possesses the same longest relaxation time as $C_{78}H_{158}$ used in the NEMD simulations [20]. The difference in computational efficiency of the NEMD and BD simulations is approximately two orders of magnitude.

3.3. Continuum level

Eqs. (34) and (36) were solved for the bead-spring chain and dumbbell models, respectively, using a Newton-Raphson algorithm to solve the nonlinear system of algebraic equations resulting from the imposition of a steady-state shearing field. The maximum extensibility of the single spring for the dumbbell model (b_s) was 20, and the ones for the bead-spring chain model (b_s) were set to 0.08889, each in dimensionless units.

3.4. Rheological and structural properties

The stress tensor is given by Kramers' expression [27], and written in dimensionless form according to the transformations of Eq. (24),

$$\tilde{\sigma}_{\alpha\beta} = \frac{1}{N-1}\sum_{i=1}^{N-1} h_i\left\langle \tilde{Q}_\alpha^i\tilde{Q}_\beta^i\right\rangle - \delta_{\alpha\beta}. \tag{40}$$

In this study, the rheological material functions play an important role in comparing results from each level of description. The viscosity and the normal stress coefficients are defined as

$$\eta = \frac{\tilde{\sigma}_{xy}}{\tilde{\dot{\gamma}}}, \tag{41}$$

$$\Psi_1 = \frac{\tilde{\sigma}_{xx} - \tilde{\sigma}_{yy}}{\tilde{\dot{\gamma}}^2}, \tag{42}$$

$$\Psi_2 = \frac{\tilde{\sigma}_{yy} - \tilde{\sigma}_{zz}}{\tilde{\dot{\gamma}}^2}. \tag{43}$$

The average conformational changes of the chain under shear flow can be expressed using various properties such as the conformation tensor, radius of gyration, orientation angle, etc. These properties can be defined as follows. The radius of gyration tensor is represented as

$$\tilde{G}_{\alpha\beta} = \frac{1}{N}\sum_{i=1}^{N}\left(\tilde{r}_\alpha^i - \tilde{r}_\alpha^c\right)\left(\tilde{r}_\beta^i - \tilde{r}_\beta^c\right), \tag{44}$$

where the position vector of the center of mass is given by,

$$\tilde{r}_\gamma^c = \frac{1}{N}\sum_{i=1}^{N}\tilde{r}_\gamma^i. \tag{45}$$

The molecular configuration thicknesses of the bead-spring chain were computed using the radius of gyration tensor, and are given by the expressions

$$\delta_x = \sqrt{\tilde{G}_{xx}},\quad \delta_y = \sqrt{\tilde{G}_{yy}},\quad \delta_z = \sqrt{\tilde{G}_{zz}}. \tag{46}$$

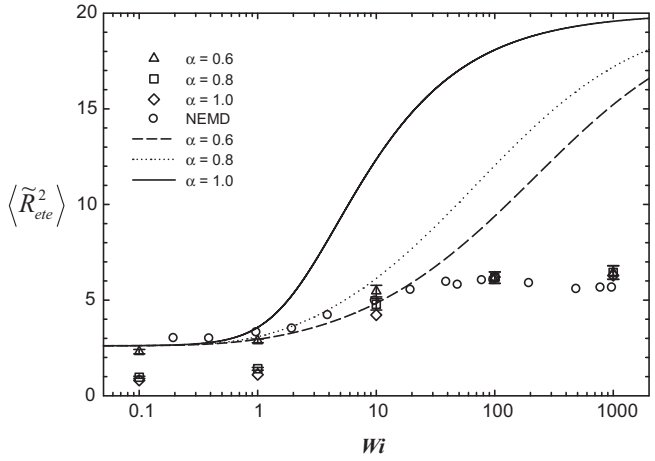

Fig. 1. The mean-square end-to-end distance, $\langle \tilde{R}^2_{ete} \rangle$, plotted as a function of *Wi* at various values of α. Note that in this and all subsequent figures, the circles denote data from the atomistic NEMD simulations of $C_{78}H_{158}$, whereas all other symbols denote results of the BD simulations at various values of α. The solid and dashed curves represent results obtained from the continuum dumbbell model.

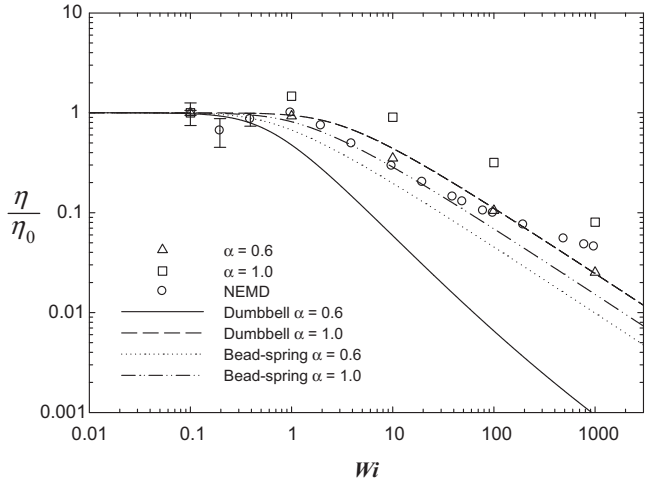

Fig. 2. The shear viscosity normalized relative to the zero-shear viscosity vs. *Wi*. Symbols and lines are as described in the caption of Fig. 1; however, additional curves are present in this figure to represent the predictions of the pre-averaged bead-spring chain model. Error bars, if not indicated, are smaller than the size of the symbols.

The orientation angle (θ) also can be calculated using the conformation tensor or the radius of gyration tensor [1,52,53] as

$$\tan(2\theta) = \frac{2\tilde{C}_{xy}}{\tilde{C}_{xx} - \tilde{C}_{yy}} = \frac{2\tilde{G}_{xy}}{\tilde{G}_{xx} - \tilde{G}_{yy}}. \quad (47)$$

4. Results and discussion

Fig. 1 displays $\langle \tilde{R}^2_{ete} \rangle$ as a function of *Wi* for the atomistic model (labeled NEMD), the mesoscopic bead-spring chain model (symbols), and the dumbbell model (curves). The NEMD atomistic data has been reported elsewhere in Refs. [19,20]. The dumbbell model values of dimensionless quantity $\langle \tilde{R}^2_{ete} \rangle$ were obtained using the standard definition $\langle \tilde{R}^2_{ete} \rangle = \tilde{\mathbf{C}} = K\mathbf{C}/k_BT$. The NEMD atomistic results have been rendered dimensionless using the standard formula $\langle \tilde{R}^2_{ete} \rangle = 3\langle R^2_{ete} \rangle / \langle R^2_{ete} \rangle_{eq}$. In order to maintain the dimensional proportionality of this quantity (see, for example, Fig. 2 of Ref. [20]), the BD results have been scaled by the same factor as the NEMD results. This data exhibits a slow initial increase at low values of *Wi*, a dramatic increase at intermediate values of *Wi*, and then a maximum and slight subsequent decrease at high *Wi*. The maximum value of $\langle \tilde{R}^2_{ete} \rangle$ is well below the fully stretched chain length, which is about 20 in dimensionless units. Kim et al. [19,20] demonstrated that this phenomenon was a direct result of the quasi-periodic tumbling of individual chain molecules, which became faster and more prevalent with increasing *Wi* beginning at a *Wi* value of about 2–4. Effectively, individual chains were diffusing through tubes formed by the highly elongated surrounding chains. The average of the highly stretched chains and the rotating chains (with very small values of $|\mathbf{R}_{ete}|$ since the chain ends pass very close to each other during the tumbling cycle [19,20]) gave a value of $\langle \tilde{R}^2_{ete} \rangle$ about 30% (at the maximum in Fig. 1; a *Wi* of about 100) of the square of the fully stretched chain length.

Results of the mesoscopic bead-spring chain BD simulations are also presented in Fig. 1 for various values of the parameter α. This parameter was varied in the range of [0.5,1.0], and three of these values are indicated in the plot. The optimal match between the atomistic data and the mesoscopic data occurs for the value $\alpha = 0.6$, indicating an especially significant degree of anisotropicity in the diffusion tensor. For this value of α, a quantitative agreement is obtained between the atomistic simulation data and the mesoscopic data, except at the highest values of *Wi* tested. This α value very nearly corresponds to Doi and Edwards' result [24] that the ratio of the perpendicular and parallel diffusion coefficients of a rod-like molecule is 0.5 in dilute and semi-dilute solutions. Henceforth, α is fixed at the value of 0.6 for all quantitative comparisons with the atomistic and experimental data based on this single comparison alone, making all further results presented below actual predictions of the mesoscopic model. Note that the value of $\langle \tilde{R}^2_{ete} \rangle$ for the BD simulations is significantly lower than that for the NEMD simulations. This is due to the absence of the excluded volume effect in the BD model [20], which is present in the atomistic simulations of these short and relatively stiff chains. As the *Wi* increases, the excluded volume effect becomes of decreasing importance. However, this quantity, $\langle \tilde{R}^2_{ete} \rangle$, would also take on the value of 3 if the data had been scaled relative to the absolute dimensional value of $\langle R^2_{ete} \rangle$ as obtained in the BD simulations.

Fig. 1 also contains data obtained from solving the anisotropic FENE dumbbell model under steady shear flow. The curves corresponding to the isotropic case ($\alpha = 1.0$) and the mildly anisotropic case ($\alpha = 0.8$) both over-predict the atomistic simulation data after a *Wi* value of approximately unity. The significantly anisotropic case ($\alpha = 0.6$), however, offers a reasonable fit of the atomistic data up to a *Wi* value of approximately 5, after which it begins to over-predict the data to a large degree. Note that all three of these cases approach the maximum value (20) of $\langle \tilde{R}^2_{ete} \rangle$ at very high values of *Wi*, and that the case of $\alpha = 0.6$ begins to differ from the atomistic data in precisely the same range of *Wi* where chain rotation and tumbling begins to play an important (and ultimately, dominating) role in the system dynamics. This provides one piece of evidence that the suppression of chain rotation through the pre-averaging process used to derive the macroscopic dumbbell model causes a loss of information concerning the bulk dynamics that is crucial to a complete and quantitative description of the fluid's rheological and kinematical responses. This is consistent with recent modeling efforts by Stephanou et al. [54], which demonstrated that $\tilde{C}_{xx} < b_m$ and $\tilde{C}_{yy}, \tilde{C}_{zz} > 0$ for large *Wi* by using a non-zero value of a slip parameter, ξ, which is known to re-introduce tumbling back into pre-averaged liquid-crystalline fluid models [3,10–13].

Fig. 2 displays the shear viscosity as a function of *Wi*. Note that viscosity is normalized with respect to its zero-shear viscosity. The shear-thinning behavior is observed at all levels of description. The mesoscopic model at $\alpha = 0.6$ is consistent with the NEMD simulation data over all values of *Wi* examined in the simulations, whereas the isotropic case ($\alpha = 1.0$) greatly over-predicts the viscosity over almost the entire *Wi* range examined.

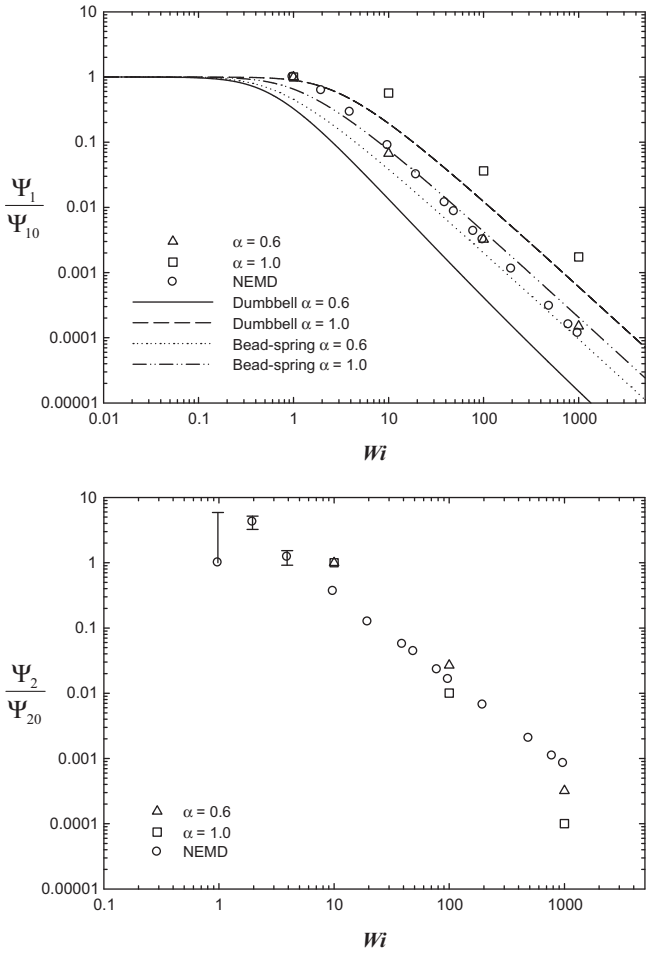

Fig. 3. The normal stress coefficients normalized relative to their zero-shear values as functions of *Wi*. Symbols and lines are defined as in previous figure captions. Error bars, if not indicated, are smaller than the size of the symbols.

The pre-averaged bead-spring model at $\alpha = 1.0$, 0.6 describes semi-quantitatively the overall behavior of the NEMD simulation data until approximately $Wi < 50$. The isotropic case actually provides a more quantitative prediction than the anisotropic case; however, this is likely just a matter of chance, since both cases of the pre-averaged bead-spring model cannot describe the chain tumbling that is dominating the rheological response of the fluid at high values of *Wi*. The dumbbell model over-predicts the data in the isotropic case, and greatly under-predicts the data in the anisotropic case.

In all of the mesoscopic and continuum models, as α decreases the viscosity becomes smaller for a given value of *Wi*. This is reasonable from a physical point of view since, as α decreases, an individual chain moves more freely along its contour, which implies that the chain will experience fewer interactions with the surrounding chains, thus reducing frictional drag. As a result, the hydrodynamic stress imposed by the shear flow decreases and therefore the viscosity decreases with decreasing α at the same value of *Wi*. The power-law index (b) was calculated at high values of *Wi* at each level of description $\left(\eta \propto \dot{\gamma}^{-b}\right)$. While the power-law index was 0.48 ± 0.02 in the range of [1,100] for the atomistic NEMD simulations, it changed with α in the mesoscopic and continuum models. In the mesoscopic bead-spring chain model and the continuum dumbbell model, the power-law index decreased from 0.58 to 0.53 and from 0.83 to 0.64 as α increased from 0.6 to 1.0, respectively. In the pre-averaged bead-spring chain model, it was approximately 0.66 for the values of α presented in the figure.

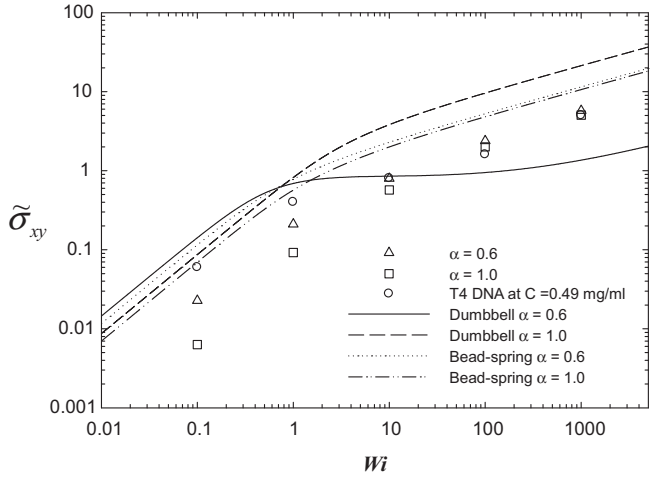

Fig. 4. Comparison of the shear stresses computed from models with experimental results of semi-dilute DNA solutions as functions of *Wi*.

Fig. 3 displays the normal stress coefficients as functions of *Wi*. From the figure, it is evident that the first normal stress coefficient, Ψ_1, and second normal stress coefficient, Ψ_2, decrease with increasing values of *Wi*. In other words, thinning behavior is observed in Ψ_1 and Ψ_2 for all models. For the first normal stress coefficient, the mesoscopic model and pre-averaged model of the bead-spring chain at $\alpha = 0.6$ capture the overall quantitative behavior of the NEMD simulation data over the entire range of *Wi*, whereas the continuum dumbbell model at the same value of α always under-predicts the NEMD simulation data. For the second normal stress coefficient, there is a remarkable overlap between the mesoscopic model at $\alpha = 0.6$ and NEMD simulation data given the inherent difficulty in calculating this quantity. The dumbbell-level model always predicts a value of zero for Ψ_2 because $\tilde{C}_{yy} = \tilde{C}_{zz}$ (see Fig. 6 below); therefore, even though these two components are decreasing as they should, $\Psi_2 = 0$. Note that this behavior is also evident in the original FENE-P dumbbell model – see Fig. 1 of Ref. [55].

For all three rheological characteristic functions examined thus far, the anisotropic mesoscopic bead-spring chain model has predicted the atomistic simulation data remarkably well for a single value of the parameter $\alpha = 0.6$, which was chosen based purely on a measurement of the mean-square end-to-end distance of the chain.

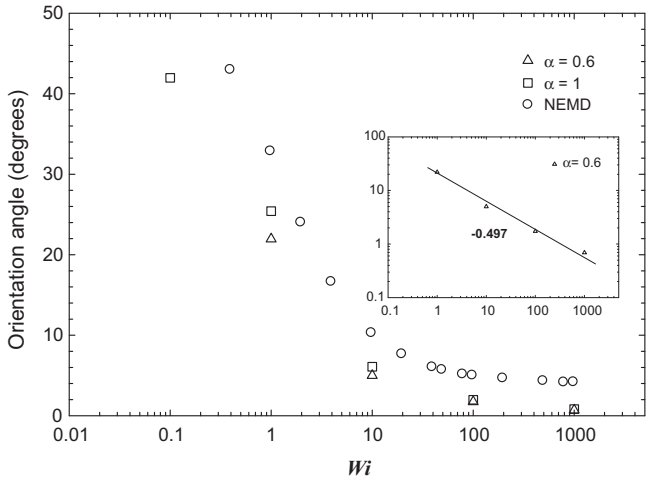

Fig. 5. The orientation angle of the mesoscopic model compared with the atomistic data as a function of α and *Wi*. The inset of this figure displays the orientation angle of mesoscopic model at $\alpha = 0.6$ vs. *Wi* on a log–log plot.

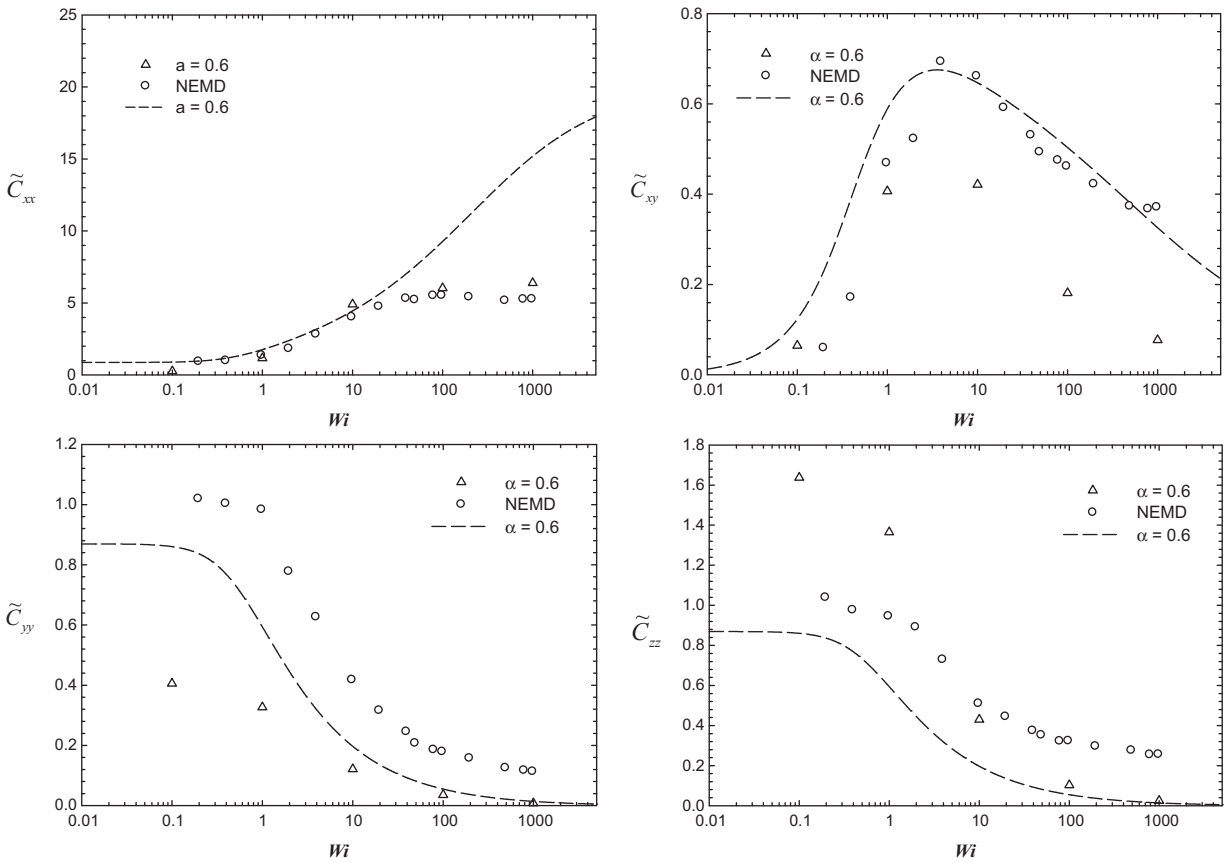

Fig. 6. The non-zero components of the conformation tensor as functions of *Wi* for the atomistic data, the mesoscopic bead-spring model, and the macroscopic dumbbell model.

This provides strong evidence that the mesoscopic model is capturing the inherent tumbling cycles of the individual chains within the atomistic fluids; this will be verified later.

The steady-state shear stresses, $\tilde{\sigma}_{xy}$, of the mesoscopic bead-spring chain and the continuum models are plotted in Fig. 4 as functions of *Wi* at various values of α. The $\tilde{\sigma}_{xy}$ of the semi-dilute T4 DNA solutions (0.49 mg/ml; 7–8 entanglements per chain) is displayed as a function of $\dot{\gamma}\tau_D$, where τ_D is disengagement time [56]. Three characteristic regions are observed in the experimental data: a low shear rate regime where the shear stress increases dramatically; an intermediate regime wherein the slope of the shear stress curve decreases dramatically, giving the appearance of a brief shear-stress plateau; and a high shear rate regime in which the shear stress resumes increasing substantially with increasing shear rate [56]. This type of intermediate and high shear behavior has been attributed in the literature as arising from a number of possible sources, including convected constraint release, reptation tube distortion, and the slipping of chain linkages.

The mesoscopic bead-spring chain model also exhibits these three characteristic regimes in the shear stress as a function of *Wi*. In the first regime, $\tilde{\sigma}_{xy}$ increases dramatically with increasing *Wi*. In the second regime, $\tilde{\sigma}_{xy}$ increases very slowly with increasing *Wi* resulting in a characteristic slight stress plateau. In the third regime, $\tilde{\sigma}_{xy}$ increases again rather quickly as *Wi* increases. This characteristic behavior of the mesoscopic model corresponds reasonably well with the experimental results of the semi-dilute DNA solutions [56] for $\alpha = 0.6$, although there are small differences in the lower shear rate regime. When $\alpha = 1.0$, the mesoscopic model predictions are much less accurate than the anisotropic version, although both models tend to converge to the same value (along with the experimental data) at the highest shear rate examined. The anisotropic model exhibits the stress plateau in the same region as the experimental data, and this occurs around $Wi = 10$, which is where the rotational motion and tumbling of the individual chains begins to have a dramatic effect on the rheological response of the test fluid. This provides another possible explanation for the occurrence of a stress plateau at intermediate shear rates. Furthermore, the isotropic model does not exhibit any hint of a stress plateau at intermediate values of *Wi*, even though tumbling of individual chains still occurs at these *Wi* values in this model. This lends credence to the hypothesis that anisotropic chain diffusion is an important part of the overall chain dynamics; i.e., the isotropic chains rotate by stretching and recoiling cycles, whereas the anisotropic chains rotate in more of the shape of a rope passing over a pulley [20]. Consequently, it is likely that the anisotropic chain rotation is somehow associated with the shear stress plateau at intermediate shear rates.

The continuum-level bead-spring chain and dumbbell models are also displayed in Fig. 4. The bead-spring chain model over-predicts the experimental data at all shear rates, and the value of the shear stress does not vary much with the parameter α. Furthermore, this model does not exhibit any hint of a shear stress plateau at intermediate values of *Wi*. The dumbbell model greatly over-predicts the experimental data for $\alpha = 1.0$, but although giving a poor quantitative prediction for $\alpha = 0.6$, it does capture the shear-stress plateau at intermediate values of shear rate and the correct qualitative behavior over the entire range of *Wi* investigated; this is possibly fortuitous.

The orientation angle, θ, of the mesoscopic bead-spring chain model is displayed in Fig. 5 as a function of *Wi* and compared with the data from the NEMD simulations. Typically, under shear flow, the orientation angle decreases from 45° with increasing shear rate, and approaches a value of a few degrees above the direction of flow

at high shear rates [1,21]. This is due to the random orientation of chains under quiescent conditions and the alignment of the chain molecules in the direction of flow at high shear rates. As shown in Fig. 5, the orientation angle follows typical behavior. It decreases from around 45° with increasing *Wi* and remains a few positive degrees above the direction of flow, on average, at high values of *Wi*. Note that the orientation angle for all α is expected to converge to 45° at low values of *Wi*. In the inset of the figure, the slope of the orientation angle at $\alpha = 0.6$ is -0.497 ± 0.04, which is very close to -0.46 ± 0.04 obtained from DNA solutions [17]. The mesoscopic model under-predicts the simulation data at all *Wi*, and rapidly asymptotes to zero degrees at extremely high shear rates. This is due to the primary difference between the two sets of simulation data: one is for a dense liquid (NEMD) and the other for a single chain in solution (BD) where the effects of surrounding chains are treated in a mean-field type of approach.

Fig. 6 displays the data for the non-zero components of the dimensionless conformation tensor, $\tilde{\mathbf{C}}$. The upper-left plot is very similar to that of Fig. 1, as expected. The atomistic NEMD simulation data is described very well by the mesoscopic bead-spring chain model with the anisotropic parameter $\alpha = 0.6$. The anisotropic dumbbell model, on the other hand greatly over-predicts the simulation data at high shear rates, and asymptotes to the fully extended value of 20. Apparently, the exclusion of the rotational chain dynamics in this pre-averaged model is responsible for this huge discrepancy between the dumbbell model and the atomistic simulation data. For the $\tilde{C}_{xy}$ component of the conformation tensor, the anisotropic dumbbell model provides a much more quantitative fit of the atomistic data (likely fortuitous), whereas the bead-spring chain fails to match the maximum quantitatively and the high shear decrease of this component. It is also obvious that $\tilde{C}_{yy}$ decreases with increasing *Wi* since the chains are compressed in flow-gradient direction under shear. The $\tilde{C}_{zz}$ component also decreases with increasing *Wi* because the chains are stretched and aligned with respect to the flow direction, again providing a compression in the neutral direction. For these two components, the mesoscopic model does not approach the unit value of either the $\tilde{C}_{yy}$ or $\tilde{C}_{zz}$ component, which is due to the fact that the parameter α is fixed to a constant value (0.6) in the simulations, whereas it should approach unity as *Wi* asymptotes to zero and the rotational motion of the chains comprising the fluid becomes isotropic. Further refinement of this model would include a *Wi*-dependent α; however, the dynamical effects of interest herein occur at high values of *Wi* where this issue is not present.

The overall quantitative predictions of the mesoscopic and dumbbell model for the $\tilde{C}_{yy}$ and $\tilde{C}_{zz}$ components are equally poor; this is probably due to the crudeness of using the conformation tensor to describe a chain molecule, especially since the atomistic chain is rather stiff while the mesoscopic chain is entirely flexible. (This is also true with respect to the orientation angle of Fig. 5.) Because of this, it is far more informative to study the radius of gyration tensor, which provides a more natural descriptor of molecular chain dynamics and shape: it is computed at each atomistic or bead location along the chain, rather than being grossly approximated as applied to only the chain termination sites.

The radius of gyration tensor provides a more natural and quantitative representation of the average size of polymeric chains. Thus, the mean configuration thickness has been calculated using the radius of gyration tensor, as in previous studies [16,17,53]. Fig. 7 shows the mean molecular configurational thickness, as computed from the mesoscopic model as a function of *Wi*. It is reasonable that the mean molecular configurational thickness in the flow direction, $\langle \tilde{\delta}_x \rangle$, exhibits very similar behavior to $\langle \tilde{R}^2_{ete} \rangle$. It maintains its equilibrium, isotropic value near the quiescent condition for all values of α. It increases rapidly at intermediate values of *Wi*, where the

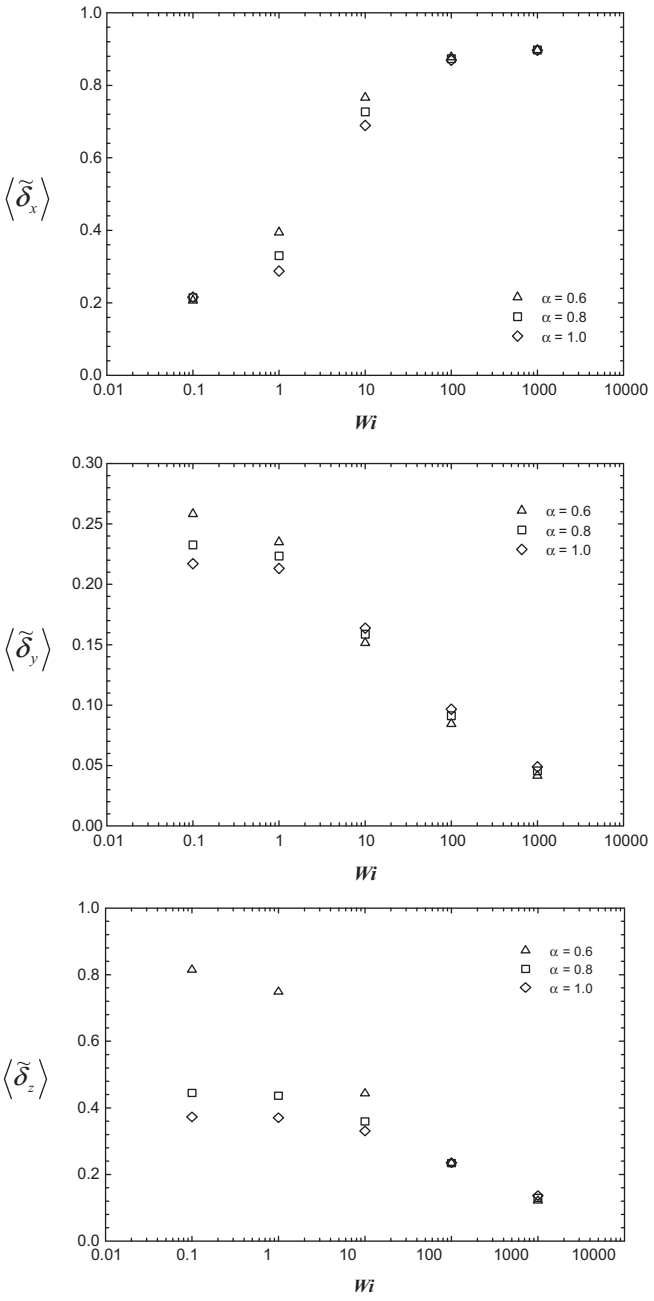

Fig. 7. Molecular configuration thicknesses in the mesoscopic model as functions of α and *Wi*.

most anisotropic case, $\alpha = 0.6$, displays the most extended configurational thickness; i.e., the chains rotate in an increasing elliptical configuration as the relative diffusion constant ratio is decreased. At high values of *Wi*, $\langle \tilde{\delta}_x \rangle$ begins to plateau, as does $\langle \tilde{R}^2_{ete} \rangle$.

It is evident that $\langle \tilde{\delta}_x \rangle$ increases with decreasing α at the same value of *Wi* because the chain moves along its contour more freely than in the perpendicular direction: consequently, the average chain maintains a more extended structure in the *x*-direction for lower values of the anisotropic parameter α. At very low *Wi*, the three cases overlap, since there is very little rotational motion and extension of the chains under weak shear and thus not much of a relative disturbing force from the equilibrium condition. The relative differences between the three cases are rather large at intermediate shear rates, but then again converge to approximately the same value at very high shear rates. This is due to the fact that at

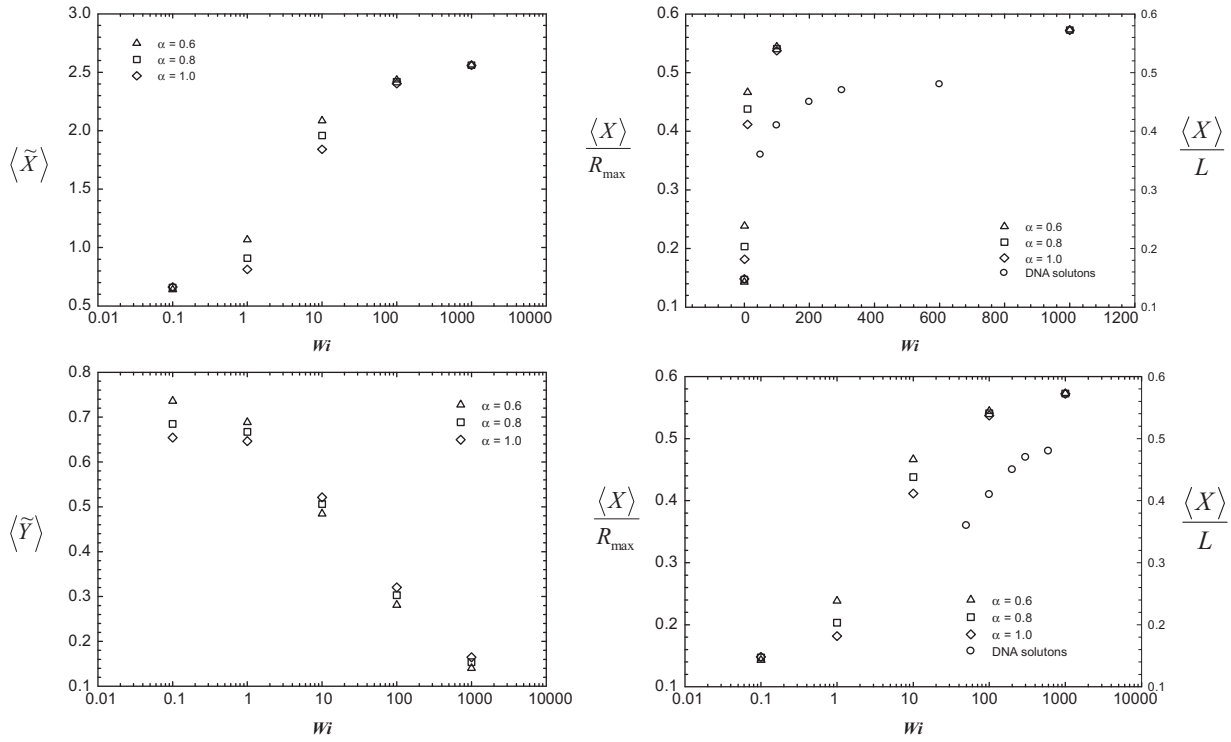

Fig. 8. The mean molecular extension in the mesoscopic model at various values of α vs. *Wi*. The scaled graphs in this figure are the mean fractional extension vs. *Wi*. Note that R_{max} is the fully stretched chain length of the bead-spring chain and L is the contour length of the DNA molecules.

high *Wi* the chains are rotating so fast that the difference between the three cases is minimized, on average.

As expected, the mean molecular configuration thicknesses in the flow-gradient direction, $\langle\tilde{\delta}_y\rangle$, and in neutral direction, $\langle\tilde{\delta}_z\rangle$, decrease with increasing *Wi*. The $\langle\tilde{\delta}_y\rangle$ and $\langle\tilde{\delta}_z\rangle$ decrease with decreasing α at intermediate and high shear rates for a given value of *Wi* for the same reasons as above; i.e., as the chains rotate in an increasingly elliptical configuration with decreasing α, there is more relative compression in the perpendicular direction. It is also interesting that the slope of $\langle\tilde{\delta}_y\rangle$ at $\alpha = 0.6$ is very close to that of the DNA solutions in a previous study [17]: they are −0.25 and −0.26, respectively. Note that the behavior of $\langle\tilde{\delta}_z\rangle$ is qualitatively the same as that of $\langle\tilde{\delta}_y\rangle$, although its value is rather high at low *Wi* and α, which is attributed to the fact that the latter parameter does not approach unity as $Wi \to 0$, as it should. As stated before, the present model was designed to describe the physics at high values of *Wi*, and therefore the parameter α was not forced to approach zero at low flow rates.

Although the end-to-end distance is one of the most useful theoretical tools in polymer dynamics, it is hard to measure it experimentally due to poor resolution and dimensional limitations of typical experimental devices. Therefore, in previous experimental studies, the projected distances between the two farthest beads to the flow-gradient and flow-vorticity planes were calculated [14–18]. In Fig. 8, the projected farthest distance between two beads on the chain at each plane is shown as a function of *Wi*. Reasonably, the overall behavior of the mean molecular extension projected onto the flow-vorticity plane, $\langle\tilde{X}\rangle$, is qualitatively similar to $\langle R^2_{ete}\rangle$ and $\langle\tilde{\delta}_x\rangle$. It increases with increasing *Wi* at low values of *Wi*. At intermediate values of *Wi*, $\langle\tilde{X}\rangle$ increases dramatically, but it does not reach the plateau value at high values of *Wi*. The $\langle\tilde{X}\rangle/\tilde{R}_{max}$ in Fig. 8 is consistent with the data of the DNA solutions [17,18], although the mean value is over-predicted by the mesoscopic model at all values of α. The mean molecular extension in the vorticity-gradient and flow-gradient planes, $\langle\tilde{Y}\rangle$ and $\langle\tilde{Z}\rangle$, display similar qualitative behavior to the $\langle\tilde{\delta}_y\rangle$ and $\langle\tilde{\delta}_z\rangle$ as functions of *Wi*: they decrease with increasing *Wi*. The dependence of the mean molecular extension, $\langle\tilde{X}\rangle$, $\langle\tilde{Y}\rangle$, and $\langle\tilde{Z}\rangle$, on α exhibits the same behavior as the mean configuration thickness, $\langle\tilde{\delta}_x\rangle$, $\langle\tilde{\delta}_y\rangle$, and $\langle\tilde{\delta}_z\rangle$, respectively.

As stated before, the dimensionless parameter α is the ratio of the perpendicular and parallel diffusion coefficients ($\alpha = \Lambda_\perp/\Lambda_{||}$). When $\alpha = 1$, the anisotropic diffusion tensor reduces to an isotropic diffusion tensor. When $0 < \alpha < 1$, parallel diffusion is preferred. Thus, it is very meaningful to examine the dependence of the probability distribution of $|\mathbf{R}_{ete}|$ on α in the mesoscopic model and to compare it with the distribution obtained from the atomistic simulation data. In Fig. 9, two values of α were chosen: one with isotropic diffusion tensor ($\alpha = 1$), and one with anisotropic diffusion tensor ($\alpha = 0.6$). For the isotropic diffusion tensor ($\alpha = 1$), the probability distributions exhibit typical overall behavior of dilute solutions [14,15,18]. It follows Gaussian behavior at low values of *Wi*, and becomes wide at intermediate values of *Wi*. At high values of *Wi*, the probability distributions display bimodal behavior with stretch and rotational peaks. For the anisotropic diffusion tensor ($\alpha = 0.6$), the probability distribution displays different behavior compared to dilute solutions or the isotropic diffusion tensor model. Although it maintains the Gaussian character at low values of *Wi*, the entire width of the distributions becomes wider and the peaks of the distributions lower in height compared to the isotropic diffusion tensor. It is reasonable that the anisotropic diffusion, where chains are diffusing along their contours, results in this change of shape of the probability distribution. Since parallel diffusion is preferred, the number of chains with extended lengths should increase. At intermediate values of *Wi*, the shape of the probability distribution is no longer Gaussian. At high values of *Wi*, the bimodal behavior is also observed with stretch and rotational peaks for the anisotropic diffusion tensor ($\alpha = 0.6$). It is very interesting that the overall behavior of the probability distribution depends on α at low and intermediate values of *Wi*, whereas it is independent of α at high values of *Wi*. This might be related to a competition between the entropic

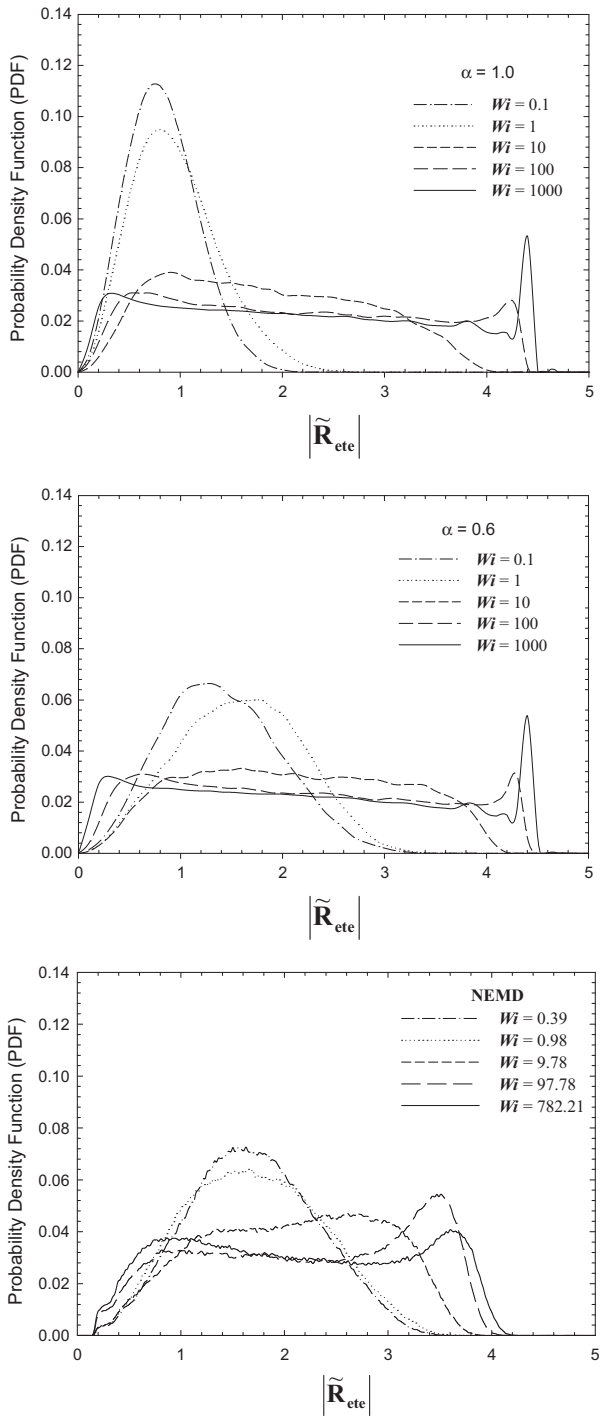

Fig. 9. The probability distribution of the atomistic NEMD simulations and the mesoscopic model vs. $|\tilde{\mathbf{R}}_{ete}|$ at various values of *Wi* and α.

spring effect (or deformation of the chains) and hydrodynamic drag imposed by shear flow (or rotational motion of the chain) on the system response. At low values of *Wi*, the system response is dominated by the entropic spring effect since the hydrodynamic drag imposed by shear flow (or vorticity) is weak. The entropic spring effect is thus strongly affected by the anisotropic diffusion matrix. Hence, the probability distribution depends to some degree on α in this *Wi* regime. However, at high values of *Wi*, the hydrodynamic drag imposed by strong shear flow overcomes the entropic spring effect. Hence, only the rotational motion of the chains dominates the system response and the probability distribution is independent of α. Thus at intermediate values of *Wi*, the competition between the two effects introduces these frozen states of the distribution for values of $\alpha < 1$, where the chain tumbling cycles offset the increased stretching of the chains.

The probability distributions of the mesoscopic model at $\alpha = 0.6$ are also compared with NEMD simulation data in this figure since it predicted well other rheological and structural properties of the NEMD simulations. As expected, the probability distributions of the mesoscopic model at $\alpha = 0.6$ show very similar behavior to the NEMD simulations. Especially, the probability distributions at low values of *Wi* considerably resemble NEMD simulation data. For example, the width of the probability distribution for $Wi = 1$ is roughly the same between the mesoscopic model and the NEMD simulations. Note that the peak is much narrower for the isotropic diffusion tensor ($\alpha = 1$) than the NEMD simulations. At intermediate values of *Wi*, the overall shape of the probability distributions are very similar between the mesoscopic model at $\alpha = 0.6$ and the NEMD simulations. However, the probability distribution of the NEMD simulations is slightly biased to higher $|\mathbf{R}_{ete}|$ as compared to the mesoscopic model. At high values of *Wi*, the bimodal behavior with stretch and rotational peaks is observed in both simulations.

Time correlation functions of the components of the end-to-end vector provide significant characteristic timescales of the system response through Fourier transform of the correlation signal. Thus, rheological and structural responses of the mesoscopic model can be compared via characteristic time scales between the mesoscopic model and NEMD simulation data. Fig. 10 displays the time correlation functions of the *xx* component of the end-to-end vector, $\tilde{\mathbf{R}}_{ete}$, as functions of observation time, $\tilde{t}$. The correlation curves of the mesoscopic model show similar behavior to the NEMD simulations at corresponding values of *Wi*. For example, the correlation curves of the mesoscopic model display the typical exponential decay for $Wi < 2$, and exhibit a characteristic minimum, local maximum, and damped oscillatory behavior at longer times for $Wi \geq 2$. Note that the slope of the decay at low values of *Wi* and the appearance of characteristic minimum at high values of *Wi* depend on α.

In Fig. 11, the characteristic timescales are displayed as functions of *Wi*. In this figure, τ_R denotes the longest relaxation time (Rouse time) and τ_{xx} refers to the characteristic timescales extracted from the correlation of the *xx* components of $\tilde{\mathbf{R}}_{ete}$. (More detailed explanations regarding characteristic timescales have been already discussed by Kim et al. [20].) For $Wi < 2$, the characteristic timescales were extracted by fitting the time correlation of the end-to-end vector with an exponential. On the other hand, the power spectral density function through Fourier transform of the correlation signal was used to extract the characteristic timescales for $Wi \geq 2$.

There are two regimes in Fig. 11. In the first regime ($Wi < 2$), the characteristic timescales of the mesoscopic model converge to the Rouse time near quiescent conditions. However, they increase with increasing *Wi* up to the unit value. In addition, the characteristic timescales become larger with decreasing α at the same value of *Wi*. This might be related to the entropic spring effect. With decreasing α, the bead-spring chain moves more easily in the parallel direction. Therefore, it starts to stretch more easily from equilibrium chain length along its backbone direction as *Wi* increases. However, the bead-spring chain stretches less in backbone direction with increasing α at the same value of *Wi*. Thus, a given chain with a smaller α value has a slightly longer correlation time. As a result, the characteristic timescales increase with decreasing α and increasing *Wi* for this regime. The previous results of the bead-rod chains in Kim et al. [20] also support this assumption. In the bead-rod chain model, the characteristic time scales maintain nearly constant values since the bead-rod chain might not admit small bond extensions caused by weak shear flow. Hence, it is reasonable that the entropic spring effect or deformation of the chains controls the

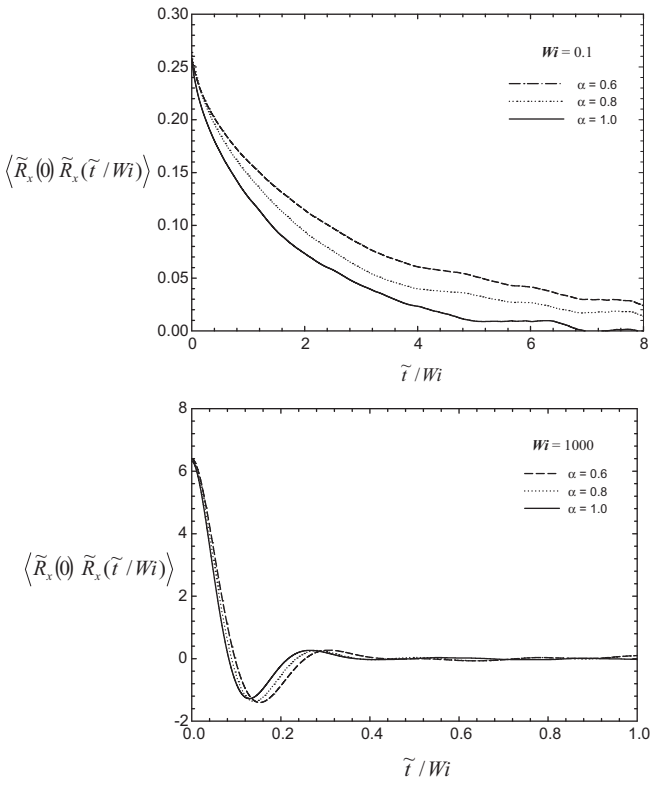

Fig. 10. The time correlation functions from the bead-spring chain BD simulations of the *xx* component of $\tilde{\mathbf{R}}_{ete}$ vs. observation time at $Wi = 0.1$ and $Wi = 1000$.

system response for $Wi < 2$ since the rotational motion of chains caused by shear flow is insignificant.

In the second regime ($Wi \geq 2$), the characteristic timescales of the mesoscopic model almost overlap with the NEMD simulation data, although the values of the timescales increase with decreasing values of α. The same explanation regarding the behavior of the probability distribution as a function of Wi can be applied here. For $Wi \geq 2$, the rotational motion of chains imposed by shear flow eventually dominates the entropic spring effect or deformation of chains on the system response at high values of Wi. Thus, the characteristic timescales eventually become almost independent of α, as noted above, since the preferential anisotropic diffusion along the chain axis is not as important to the dynamical tumbling cycles.

According to Doi and Edwards [24], the characteristic time scales, τ_{xx} and τ_{yy}, can be related to the parallel and perpendicular diffusion coefficients, respectively. In Doi and Edwards' results for rod-like polymers in dilute and semi-dilute solutions, the ratio of the parallel and perpendicular diffusion coefficients is 0.5 [24]. The ratio of τ_{xx} and τ_{yy} obtained from NEMD simulation is 0.6–0.7, which is very close to Doi and Edwards' result. Furthermore, this ratio is also very similar to $\alpha = 0.6$ for the mesoscopic model which captures well the NEMD simulation data. Thus, it is reasonable that the characteristic time scale τ_{xx} is related to parallel diffusion and the characteristic time scale τ_{yy} corresponds to perpendicular diffusion.

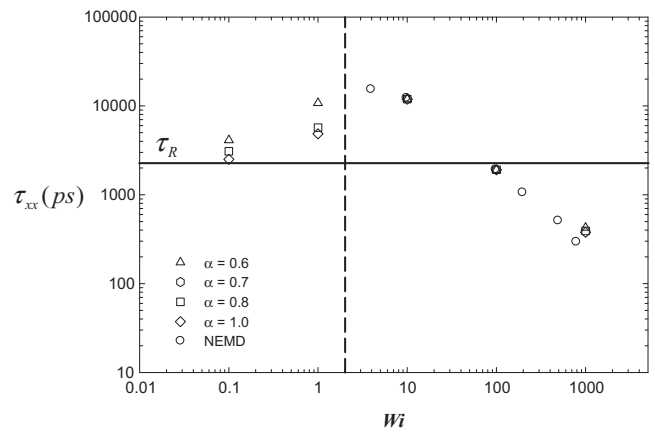

Fig. 11. The characteristic time scale, τ_{xx}, as a function of Wi for the atomistic liquid and the bead-spring chain at various values of α.

5. Conclusion

In order to clarify the dynamics of polymeric materials which often hides behind enormously complicated information under shear flow, the simple coarse-grained mesoscopic model was proposed based on a bead-spring chain with FENE springs and an anisotropic diffusion matrix. This model was further coarse-grained to bead-spring chain and dumbbell continuum models through pre-averaging and closure approximations. The rheological and structural properties of polymeric materials, such as viscosity, normal stress coefficients, mean-square end-to-end distance, and so on, computed from the simple mesoscopic and continuum models were compared with NEMD simulation data at the atomistic level and experiments of semi-dilute DNA solutions.

The $\langle \tilde{R}^2_{ete} \rangle$ computed from the NEMD simulations at the atomistic level were consistent with the $\langle \tilde{R}^2_{ete} \rangle$ at $\alpha = 0.6$ in mesoscopic model over all ranges of Wi examined in these simulations. This value of the anisotropic parameter was then used to predict the rheological and structural properties of short-chain polyethylene liquids under steady-shear flow with good success. However, the $\langle \tilde{R}^2_{ete} \rangle$ at $\alpha = 0.6$ in the dumbbell model diverged from atomistic model after $Wi = 10$, and reached the fully stretched chain length at high values of Wi due to lack of information regarding the rotational motion of the chains caused by pre-averaging.

The shear stresses computed from mesoscopic and continuum models were also compared with experimental results of semi-dilute DNA solutions. The variation of shear stress with values of α at the same value of Wi was also investigated in mesoscopic and continuum models. The $\tilde{\sigma}_{xy}$ of the mesoscopic model was dependent on α at low values of Wi while it was independent of α at high values of Wi. The values of $\tilde{\sigma}_{xy}$ at $\alpha = 0.6$ in the mesoscopic model were very similar to experimental results of DNA solutions.

The orientation angle for all α in mesoscopic model displayed the typical behavior. It decreased from 45° as the values of Wi were increased and eventually assumed a small positive angle with respect to flow direction. The orientation angle at $\alpha = 0.6$ in the mesoscopic model followed as $\langle \theta \rangle \propto Wi^{-0.497 \pm 0.04}$ and is consistent with the results of DNA solutions, which is given as $\langle \theta \rangle \propto Wi^{-0.46 \pm 0.04}$ [17].

The mean configuration thickness and mean molecular extension in the mesoscopic model showed similar behavior as functions of Wi. The $\langle \tilde{\delta}_x \rangle$ and $\langle \tilde{X} \rangle$ increased with increasing Wi, while other components decreased. Note that the overall behavior of $\langle \tilde{X} \rangle / \tilde{R}_{max}$ and, especially, the slope of $\langle \tilde{\delta}_y \rangle$ at $\alpha = 0.6$, were very close to previous studies on DNA solutions [17]. The trends of these properties caused by changing value of α was similar to that of $\langle \tilde{R}^2_{ete} \rangle$.

The characteristic timescales or tumbling frequencies were extracted from time correlation functions of components of the end-to-end vector, and were plotted as functions of Wi. The behavior of characteristic timescales was divided based on $Wi = 2$. For $Wi < 2$, the characteristic timescales recovered the Rouse time near equilibrium, and showed a dependence on α. However, for $Wi \geq 2$, the characteristic timescales for each α overlapped and displayed

very close values to those obtained from the NEMD simulation data.

Acknowledgement

This work was made possible by the National Science Foundation under Grant No. CBET-0742679 by using the resources of the PolyHub Virtual Organization.

References

[1] M. Kröger, Models for Polymeric and Anisotropic Liquids, Springer, Berlin, 2005.
[2] B.J. Edwards, H.C. Öttinger, Time/structure invariance criteria for closure approximations, Phys. Rev. E 56 (1997) 4097–4103.
[3] B.J. Edwards, Evaluation of the thermodynamic consistency of closure approximations in several models proposed for the description of liquid crystalline dynamics, J. Non-Equilib. Thermodyn. 27 (2002) 5–24.
[4] G. Marrucci, Tumbling regime of liquid-crystalline polymers, Macromolecules 24 (1991) 4176–4182.
[5] S.G. Advani, C.L. Tucker III, Closure approximations for three dimensional structural tensors, J. Rheol. 34 (1990) 367–386.
[6] E.J. Hinch, L.G. Leal, Constitutive equations in a suspension mechanics. Part 2. Approximate forms for a suspension of rigid particles affected by Brownian rotations, J. Fluid Mech. 76 (1976) 187–208.
[7] N.J. Wagner, H.C. Öttinger, B.J. Edwards, Generalized Doi-Ohta model for multiphase flow developed via GENERIC, AIChE J. 45 (1999) 1169–1181.
[8] M. Doi, Molecular dynamics and rheological properties of concentrated solutions of rodlike polymers in isotropic and liquid crystalline phases, J. Polym. Sci.: Polym. Phys. 19 (1981) 229–243.
[9] R.G. Larson, H.C. Öttinger, Effect of molecular elasticity on out-of-plane orientations in shearing flows of liquid crystalline polymers, Macromolecules 24 (1991) 6270–6282.
[10] B.J. Edwards, The dynamical continuum theory of liquids crystals, Ph.D. Dissertation, University of Delaware, 1991.
[11] B.J. Edwards, A.N. Beris, M. Grmela, The dynamical behavior of liquid crystals: a continuum description through generalized brackets, Mol. Cryst. Liq. Cryst. 201 (1991) 51–86.
[12] N.C. Andrews, B.J. Edwards, A.J. McHugh, Continuum dynamic behavior of homogeneous liquid-crystalline polymers under the imposition of shear and magnetic fields, J. Rheol. 39 (1995) 1161–1182.
[13] N.C. Andrews, A.J. McHugh, B.J. Edwards, Out-of-plane orientational dynamics of polymeric liquid crystals under flow, J. Rheol. 40 (1996) 459–469.
[14] D.E. Smith, H.P. Babcock, S. Chu, Single-polymer dynamics in steady shear flow, Science 283 (1999) 1724–1727.
[15] J.S. Hur, E.S.G. Shaqfeh, H.P. Babcock, D.E. Smith, S. Chu, Dynamics of dilute and semi-dilute DNA solutions in the start-up of shear flow, J. Rheol. 45 (2001) 421–450.
[16] C.M. Schroeder, R.E. Teixeira, E.S.G. Shaqfeh, S. Chu, Characteristic periodic motion of polymers in shear flow, Phys. Rev. Lett. 95 (2005) 018301.
[17] R.E. Teixeira, H.P. Babcock, E.S.G. Shaqfeh, S. Chu, Shear thinning and tumbling dynamics of single polymer in the flow-gradient plane, Macromolecules 38 (2005) 581–592.
[18] R.E. Teixeira, A.K. Dambal, D.H. Richter, E.S.G. Shaqfeh, S. Chu, The individualistic dynamics of entangled DNA in solution, Macromolecules 40 (2007) 2461–2476.
[19] J.M. Kim, B.J. Edwards, B. Khomami, D.J. Keffer, Single-chain dynamics of linear polyethylene liquids under shear flow, Phys. Lett. A 373 (2009) 769–772.
[20] J.M. Kim, B.J. Edwards, D.J. Keffer, B. Khomami, Dynamics of individual molecules of linear polyethylene liquids under shear: atomistic simulation and comparison with a free-draining bead-rod chain, J. Rheol. 54 (2010) 283–310.
[21] C. Baig, B.J. Edwards, D.J. Keffer, A molecular dynamics study of the stress-optical behavior of a linear short-chain polyethylene melt under shear, Rheol. Acta 46 (2007) 1171–1186.
[22] J.M. Kim, D.J. Keffer, B.J. Edwards, Visualization of conformational changes of linear short-chain polyethylenes under shear and elongational flows, J. Mol. Graph. Model. 26 (2008) 1046–1056.
[23] J.M. Kim, D.J. Keffer, M. Kröger, B.J. Edwards, Rheological and entanglement characteristics of linear chain polyethylene liquids in planar couette and planar elongational flows, J. Non-Newton. Fluid Mech. 152 (2008) 168–183.
[24] M. Doi, S.F. Edwards, The Theory of Polymer Dynamics, Clarendon Press, Oxford, 1986.
[25] A.N. Beris, B.J. Edwards, Thermodynamics of Flowing Systems, Oxford University Press, New York, 1994.
[26] T. Shimada, M. Doi, K. Okano, Concentration fluctuation of stiff polymers. III. Spinodal decomposition, J. Chem. Phys. 88 (1988) 7181–7186.
[27] R.B. Bird, C.F. Curtiss, R.C. Armstrong, O. Hassager, Dynamics of Polymeric Liquids, vol. II, Wiley, New York, 1987.
[28] A.N. Beris, B.J. Edwards, Poisson bracket formulation of incompressible flow equations in continuum mechanics, J. Rheol. 34 (1990) 55–78.
[29] A.N. Beris, B.J. Edwards, Poisson bracket formulation of viscoelastic flow equations of differential type: a unified approach, J. Rheol. 34 (1990) 503–538.
[30] H. Giesekus, Die Elastizität von Flüssigkeiten, Rheol. Acta 5 (1966) 37–65.
[31] H. Giesekus, A unified approach to a variety of constitutive models for polymer fluids based on the concept of configuration-dependent molecular mobility, J. Non-Newton. Fluid Mech. 11 (1982) 69–109.
[32] R.B. Bird, J.R. Deaguiar, An encapsulated dumbbell model for concentrated polymer solutions and melts. I. Theoretical development and constitutive equation, J. Non-Newton. Fluid Mech. 13 (1983) 149–160.
[33] N. Phan-Thien, J.D. Atkinson, A note on the encapsulated dumb-bell model, J. Non-Newton. Fluid Mech. 17 (1985) 111–116.
[34] H.C. Öttinger, Consistently averaged hydrodynamic interaction for Rouse dumbbells in steady shear flow, J. Chem. Phys. 83 (1985) 6535–6536.
[35] J.I. Siepmann, S. Karaboni, B. Smit, Simulating the critical behaviour of complex fluids, Nature 365 (1993) 330–332.
[36] W.L. Jorgensen, J.D. Madura, C.J. Swenson, Optimized intermolecular potential functions for liquid hydrocarbons, J. Am. Chem. Soc. 106 (1984) 6638–6646.
[37] R.G. Larson, Constitutive Equations for Polymer Melts and Solutions, Butterworth-Heinemann, London, 1988.
[38] H.C. Öttinger, Stochastic Processes in Polymeric Fluids, Springer, Berlin, 1996.
[39] P.E. Rouse Jr., A theory of the linear viscoelastic properties of dilute solutions of coiling polymers, J. Chem. Phys. 21 (1953) 1272–1280.
[40] B.J. Edwards, M. Dressler, A reversible problem in non-equilibrium thermodynamics: Hamiltonian evolution equations for non-equilibrium molecular dynamics simulations, J. Non-Newton. Fluid Mech. 96 (2001) 163–175.
[41] C. Baig, B.J. Edwards, D.J. Keffer, H.D. Cochran, A proper approach for nonequilibrium molecular dynamics simulations of planar elongational flow, J. Chem. Phys. 122 (2005) 114103.
[42] B.J. Edwards, C. Baig B.J, D.J. Keffer, A validation of the p-SLLOD equations of motion for homogeneous steady-state flows, J. Chem. Phys. 124 (2006) 194104.
[43] S. Nosé, A molecular dynamics method for simulations in the canonical ensemble, Mol. Phys. 52 (1984) 255–268.
[44] W.G. Hoover, Canonical dynamics: equilibrium phase-space distributions, Phys. Rev. A 31 (1985) 1695–1697.
[45] M. Tuckerman M, B.J. Berne, G.J. Martyna, Reversible multiple time scale molecular dynamics, J. Chem. Phys. 97 (1992) 1990–2001.
[46] A.W. Lees, S.F. Edwards, The computer study of transport processes under extreme conditions, J. Phys. C: Solid State Phys. 5 (1972) 1921–1929.
[47] G. Williams, D.C. Watts, Non-symmetrical dielectric relaxation behaviour arising from a simple empirical decay function, Trans. Faraday Soc. 66 (1970) 80–85.
[48] G. Williams, D.C. Watts, S.B. Dev, A.M. North, Further considerations of non symmetrical dielectric relaxation behaviour arising from a simple empirical decay function, Trans. Faraday Soc. 67 (1971) 1323–1335.
[49] G. Tsolou, V.G. Mavrantzas, D.N. Theodorou, Detailed atomistic molecular dynamics simulation of *cis*-1,4-poly(butadiene), Macromolecules 38 (2005) 1478–1492.
[50] L.A. Deschenes, D.A. van den Bout, Single-molecule studies of heterogeneous dynamics in polymer melts near the glass transition, Science 292 (2001) 255–258.
[51] M. Somasi, B. Khomami, N.J. Woo, J.S. Hur, E.S.G. Shaqfeh, Brownian dynamics simulations of bead-rod and bead-spring chains: numerical algorithms and coarse-graining issues, J. Non-Newton. Fluid Mech. 108 (2002) 227–255.
[52] S. Hess, Rheological properties via nonequilibrium molecular dynamics: from simple towards polymeric liquids, J. Non-Newton. Fluid Mech. 23 (1987) 305–319.
[53] D.G. Thomas, R.J. DePuit, B. Khomami, Dynamic simulations of individual macromolecules in oscillatory shear flow, J. Rheol. 53 (2009) 275–291.
[54] P.S. Stephanou, C. Baig, V.G. Mavrantzas, A generalized differential constitutive equation for polymer melts based on principles of non-equilibrium thermodynamics, J. Rheol. 53 (2009) 309–337.
[55] C. Baig, B. Jiang, B.J. Edwards, D.J. Keffer, H.D. Cochran, A comparison of simple rheological models and simulation data of n-hexadecane under shear and elongational flows, J. Rheol. 50 (2006) 625–640.
[56] D. Jary, J.-L. Sikorav, D. Lairez, Nonlinear viscoelasticity of entangled DNA molecules, Europhys. Lett. 46 (1999) 251–255.